Observation of jet stream winds during NAWDEX and characterization of systematic meteorological analysis errors

Article

Accepted Version

It is advisable to refer to the publisher's version if you intend to cite from the work. See Guidance on citing.
Published version at: http://dx.doi.org/10.1175/MWR-D-19-0229.1
To link to this article DOI: http://dx.doi.org/10.1175/MWR-D-19-0229.1

CentAUR

Central Archive at the University of Reading

Reading's research outputs online

Observation of jet stream winds during NAWDEX and characterization of systematic meteorological analysis errors

Andreas Schäfler
Deutsches Zentrum für Luft- und Raumfahrt, Institut für Physik der Atmosphäre, Oberpfaffenhofen, Germany

Ben Harvey
National Centre for Atmospheric Science, University of Reading, Reading, United Kingdom

John Methven
Department of Meteorology, University of Reading, Reading, United Kingdom

James D. Doyle
Naval Research Laboratory, Monterey, California

Stephan Rahm
Deutsches Zentrum für Luft- und Raumfahrt, Institut für Physik der Atmosphäre, Oberpfaffenhofen, Germany

Oliver Reitebuch
Deutsches Zentrum für Luft- und Raumfahrt, Institut für Physik der Atmosphäre, Oberpfaffenhofen, Germany

Fabian Weiler
Deutsches Zentrum für Luft- und Raumfahrt, Institut für Physik der Atmosphäre, Oberpfaffenhofen, Germany

Benjamin Witschas
Deutsches Zentrum für Luft- und Raumfahrt, Institut für Physik der Atmosphäre, Oberpfaffenhofen, Germany

Contact:
Dr. Andreas Schäfler
Deutsches Zentrum für Luft- und Raumfahrt e.V. (DLR)
Institut für Physik der Atmosphäre
Oberpfaffenhofen, 82234 Weßling
andreas.schaefler@dlr.de

30 **Abstract**

31 Observations across the North Atlantic jet stream with high vertical resolution are used to

32 explore the structure of the jet stream, including the sharpness of vertical wind shear changes

33 across the tropopause and the wind speed. Data was obtained during the North Atlantic

34 Waveguide and Downstream impact EXperiment (NAWDEX) by an airborne Doppler wind

35 lidar, dropsondes and a ground-based Stratosphere-Troposphere radar. During the campaign

36 small wind speed biases throughout the troposphere and lower stratosphere of only -0.41 m s^{-1}

37 and -0.15 m s^{-1} are found respectively in the ECMWF and UK Met Office analyses and short-

38 term forecasts. However, this study finds large and spatially coherent wind errors up to ± 10 m s^{-1}

39 for individual cases, with the strongest errors occurring above the tropopause in upper-level

40 ridges.

41 ECMWF and Met Office analyses indicate similar spatial structures in wind errors, even

42 though their forecast models and data assimilation schemes differ greatly. The assimilation of

43 operational observational data brings the analyses closer to the independent verifying

44 observations but it cannot fully compensate the forecast error. Models tend to underestimate the

45 peak jet stream wind, the vertical wind shear (by a factor of 2-5) and the abruptness of the

46 change in wind shear across the tropopause, which is a major contribution to the meridional

47 potential vorticity gradient. The differences are large enough to influence forecasts of Rossby

48 wave disturbances to the jet stream with an anticipated effect on weather forecast skill even on

49 large scales.

1. Introduction

The existence and behavior of the North Atlantic jet stream is central to the weather experienced across Europe in all seasons. Weather systems having major impacts on surface conditions, such as mid-latitude cyclones, the fronts embedded within them and mesoscale convective systems, are all influenced strongly by interaction with the jet stream. Their structure and evolution is affected by the location of strong vertical wind shear, as well as wave and vortex disturbances at tropopause level that develop as the jet stream meanders and contorts. Meandering jet streams coincide with strong gradients of potential vorticity (PV) along the isentropic surfaces intersecting the tropopause. These gradients serve as a waveguide for propagating Rossby waves (Hoskins and Ambrizzi, 1993; Schwierz et al. 2004; Martius et al. 2010). Disturbances to the waveguide at the entrance (western) end of the storm track can have a major effect on surface weather thousands of kilometers downstream through the propagation of disturbance energy in the form of Rossby wave packets (see recent review by Wirth and Riemer, 2018). Therefore, a detailed representation of the jet stream structure is important not only locally in forecasting upper-tropospheric winds, but also has far-reaching consequences for predicting surface weather system development.

Accurate prediction of Rossby waves is sensitive to the representation of the jet stream structure and associated PV gradient, even though their wavelength exceeds the width of the strongest PV gradient regions by several orders of magnitude. This introduces a resolution dependence to jet stream prediction. It has been demonstrated that global numerical weather prediction (NWP) models fail to maintain sufficiently sharp PV gradients at the tropopause and Rossby wave amplitude decreases with lead time (Gray et al. 2014; Saffin et al. 2017). If the PV gradient is too smooth in a model then advection of disturbances by the jet stream and counter-

73   propagation of Rossby waves against the zonal flow are both expected to be too weak. Harvey et

74   al. (2016) showed analytically that although these effects on Rossby wave phase speed cancel to

75   first order, in more accurate estimates phase speed must always decrease (slower eastward).

76   Harvey et al. (2018) used wave activity theory to show that when the PV gradient is too smooth

77   in a model, then Rossby wave amplitude is also predicted to decay. The lead-time dependence of

78   the PV gradient forecast error, both in horizontal gradient along an isentropic surface (Gray et al.

79   2014) and vertical gradient (Saffin et al. 2017), indicates that the NWP models struggle to

80   represent the tropopause, an issue that is expected to be even more prominent in climate

81   prediction models due to their lower spatial resolution. Davies and Didone (2013) showed how

82   forecast errors of PV propagate and amplify along the jet stream waveguide and Baumgart et al.

83   (2018) have quantified the extent to which different dynamical mechanisms contribute to the

84   growth of PV forecast error from uncertainty in the initial conditions.

85   In this study we examine high resolution observations of the jet stream (detailed in Section

86   2) and compare them with the representation of jet-stream winds in meteorological analyses and

87   short-term forecasts. It is an open question to what extent they are able to represent the observed

88   wind speed distribution, especially the strength of the vertical wind shear on either side of the

89   tropopause, which is of crucial importance for an accurate representation of the meridional PV

90   gradient and Rossby wave evolution.

91   In the 1990s and early 2000s, several studies that used in situ observed winds onboard

92   commercial airliners to validate NWP winds reported on significant wind speed biases in

93   meteorological analyses (Tenenbaum 1991, 1996; Rickard et al. 2001; Cardinali et al. 2003).

94   Multi-case averaging revealed wind speed biases increasing with observed wind speeds and

95   reaching values of up to 5-10 % (Rickard et al. 2001). Cardinali et al. (2003) found that jet streak

96   winds are too weak by 2 to 5 % in data-dense regions over the US and by 5 to 9 % in data-sparse

97   regions over Canada. The continuous increase of vertical and horizontal resolution in NWP

98   models, the continuous increase in quality, amount and resolution of aircraft and satellite

99   observations and their improved application has led to a substantially improved representation of

100 winds in NWP analyses. As depicted by Petersen (2016), Northern Hemispheric wind errors

101 decreased by about 40% for 24-h forecasts between 1984 and 2004. Houchi et al. (2010)

102 compared winds in different climate regions using high vertical-resolution radiosondes from 85

103 stations and ECMWF short-term forecasts in the year 2006. They found qualitative agreement of

104 observed and modelled wind distributions at all levels. However, they note a substantial

105 underestimation of vertical wind shear and its variability associated with small scale vertical

106 wind gradients that are not well represented by ECMWF short-term forecasts, particularly due to

107 the limited vertical resolution of the model. Based on multi-month analysis differences between

108 ECMWF and the National Centers for Environmental Prediction (NCEP), Baker et al. (2014)

109 estimate an uncertainty of winds at 300 hPa in the order of 2-3 m s^{-1} over the northern North

110 Atlantic. More recently, Belmonte Rivas and Stoffelen (2019) compared surface winds

111 represented by ERA5 with Advanced Scatterometer (ASCAT) observations, and found

112 systematic circulation errors, in the sense that surface winds are too cyclonic across ocean basins

113 in the re-analysis and meridional winds are too weak in mid-latitudes. These surface wind errors

114 were attributed to underestimation in directional wind turning (the Ekman spiral) across the

115 boundary layer of the ECMWF model. Therefore, it can be anticipated that errors at tropopause

116 level will not have the same characteristics as surface wind errors.

117   In this study we compare operational meteorological analyses and short-term forecasts of

118 two global NWP centers, the ECMWF and the United Kingdom Met Office, with a unique set of

119   wind profile observations across the tropopause that was obtained during the North Atlantic

120   Waveguide and Downstream impact EXperiment (NAWDEX). NAWDEX was conducted in

121   autumn 2016 with the aim to examine the structure of the jet stream, the impact of diabatic

122   processes on the jet stream disturbances and their influence on high-impact weather downstream

123   (Schäfler et al. 2018). For the first time, an established Doppler wind lidar payload onboard the

124   research aircraft DLR Falcon performed dedicated observations of the jet stream winds providing

125   both high vertical and horizontal resolution, which is not available from other observational

126   sources. Additionally, the wind lidar data set is supplemented by dropsonde and ground-based

127   wind profiler observations to provide a wider coverage and to investigate the observational

128   reliability of the wind lidar.

129   In Section 2 we provide an overview of the observation and model data and the methods

130   applied to validate analyses and short-term forecasts of ECMWF and Met Office. In Section 3, a

131   case study is presented with coordinated wind lidar and dropsonde observations of a jet stream

132   near Iceland on 23 September 2016. Section 4 contains a statistical evaluation of the horizontal

133   wind and vertical wind shear representation during the NAWDEX field phase based on the wind

134   lidar data set and wind profiler observations. Discussion of the results and conclusions are given

135   in Section 5. The implications of the findings are presented in Section 6.

136   **2. Data and methods**

137   *a. Airborne observations: Doppler Wind Lidar and Dropsondes*

138   During NAWDEX, wind observations onboard the DLR Falcon were obtained by two

139   Doppler wind lidar systems; the ALADIN Airborne Demonstrator (A2D, Reitebuch et al. 2009;

140   Lux et al. 2018, Marksteiner et al. 2018) and the 2-μm Doppler wind lidar system (Weissmann et

141   al. 2005, Witschas et al. 2017). In this study we rely on observations of the horizontal wind

142   vector measured by the 2-µm Doppler wind lidar (in the following abbreviated as DWL).

143   Additionally, we use wind observations measured by in situ sensors in the nose-boom of the

144   aircraft and by dropsondes that were released during coordinated flights with the High Altitude

145   and Long Range Research Aircraft (HALO; Schäfler et al. 2018).

146   The coherent and heterodyne detection DWL measures range resolved profiles of the

147   horizontal wind vector beneath the aircraft through detection of frequency shifts between emitted

148   and retrieved laser signals. The DWL uses a wavelength of 2022.54 nm in an atmospheric

149   window with low absorption of water vapor enabling wind measurements up to the maximum

150   flight altitude of ~12 km, depending on aerosol column beneath. The DWL transmits short laser

151   pulses with a length of 400-500 ns, a repetition rate of 500 Hz and an energy of 1-2 mJ to the

152   atmosphere beneath the aircraft. The signal is partly scattered back to the aircraft by aerosols and

153   cloud particles where it is received by a telescope and analyzed for frequency shift Δf which is

154   proportional to the wind speed v_{LOS} in the line of sight (LOS) according to $\Delta f = (2f_0 \cdot v_{LOS})/c$,

155   where f_0 is the laser frequency, c is the speed of light and $\lambda_0 = c/f_0 = 2022.54$ nm is the laser

156   wavelength. To be able to derive a horizontal wind vector from LOS measurements, the DWL

157   uses a double-wedge scanner to measure LOS winds at different pointing directions. A conical

158   step-and-stare scan pattern (Velocity Azimuth Display (VAD)-technique) around the vertical

159   axes with an off-nadir angle of 20° provides 21 LOS observations per one scanner revolution. A

160   mean wind vector in the measurement volume can be derived by combining these 21 LOS

161   velocities at different viewing direction. A wind profile is derived every 42s, i.e. the time that is

162   required for one complete scanner revolution with 21 LOS observations including an averaging

163   of 1s per LOS position and the scanner movement. Wind vectors are derived at a vertical

164 resolution of 100 m. For a more detailed instrument description of the DWL and the algorithms

165 for the wind retrieval the interested reader is referred to Witschas et al. (2017).

166 During NAWDEX, the DLR Falcon successfully observed approaching cyclones and

167 evolving jet streams surrounding Iceland. Eight flights were performed with the DWL between

168 17 September and 9 October 2016 (see Fig. 1a and overview in Schäfler et al. 2018)

169 corresponding to a total measurement time of 22:55 h and a total distance of ~17,000 km. In a

170 total of 1922 measurement profiles between 0 km and 12 km altitude, 77541 horizontal wind

171 measurements were obtained which corresponds to a total data availability of about 33.8 %

172 resulting from low concentration of the required aerosol or cloud scatterers in the frequently

173 sampled clean and dry tropospheric and lower stratospheric air at high latitudes. However, the

174 NAWDEX data set provides a maximum in data availability where the average wind shows a

175 maximum, between 8 km and 10 km altitude (Fig. 1b). The maximum data availability of 80 %

176 at 9.4 km altitude corresponds to ~18:20 h of observations and a flight distance of 13,500 km.

177 The mean profile separation, i.e. the horizontal resolution, which depends on the speed of the

178 aircraft and the time for one scanner revolution (~42 s) is approximately 8.6 km. The distribution

179 of all observations shows that winds up to 91 m s^{-1} were sampled which represents the highest

180 wind speeds that have been observed by the DWL since its first airborne deployment in 2001.

181 To assess the accuracy (systematic error) and precision (random error) of the DWL during

182 the campaign, typically comparisons with independent observation types are conducted. During

183 three DLR Falcon research flights (RF02, RF03 and RF04) on 17, 21 and 23 September,

184 coordinated flights with HALO provide 15 dropsondes that are used for a comparison with DWL

185 winds. Dropsondes are small instrument carriers consisting of temperature, pressure and

186 humidity sensors as well as a GPS receiver that transmit their data to the Airborne Vertical

187 Atmospheric Profiling Systems (AVAPS; UCAR/NCAR 1993; Hock and Franklin 1999)

188 onboard the aircraft that consists of a data acquisition and processing unit. AVAPS is a well-

189 established dropsonde system to provide high quality and high resolution profile data from the

190 flight altitude down to the ground (e.g., Wang et al. 2015). During NAWDEX the Vaisala

191 dropsonde version RD94 was used (Vaisala 2017) and the data was quality-controlled using the

192 automatic post-processing Earth Observing Laboratory (EOL) Atmospheric Sounding Processing

193 Environment (ASPEN, https://www.eol.ucar.edu/software/aspen) software. Wind speed accuracy

194 is in the order of 0.2-0.3 m s^{-1} (Holger Vömel 2019, personal communication).

195 The dropsonde wind observations were vertically interpolated to the DWL vertical

196 resolution of 100 m and after accounting for the drift of the dropsonde, the spatially closest DWL

197 observation was used for comparison. Figure 1c shows a scatter plot for 529 pairs of wind

198 observations from the DWL and dropsondes ranging between 4 m s^{-1} and 55 m s^{-1}. Although, the

199 mean horizontal distance between sets of the compared observations is 10.8 km and maximum

200 distances up to 29 km are reached, no dependence on the distance difference between both

201 observations is discernible. The good agreement is reflected by a high correlation coefficient of

202 0.99. A linear fit reveals a slope value of 0.99 and an intercept of -0.004 m s^{-1}. The mean bias is

203 0.05 m s^{-1} and the standard deviation is 1.87 m s^{-1}. A more restrictive selection of data points,

204 with a maximum horizontal distance between dropsonde and DWL of 10 km leads to a reduced

205 number of 245 observations for the comparison and a reduced standard deviation of 1.50 m s^{-1}.

206 These results are in agreement with earlier findings that are summarized in Table 1 following

207 Witschas et al. (2020). Slight differences between the different campaigns may arise from

208 different weather situations and related wind variability and aerosol loads resulting in different

209 signal-to-noise ratios, differences in the retrieval algorithms and quality-control thresholds, or

210 differences in the spatial-temporal collocation. Nevertheless, these results demonstrate the high

211 accuracy and precision of the DWL.

212 *b. Wind profiler data at South Uist*

213   In addition to the airborne observations described above, the stratospheric-tropospheric wind

214 profiler (STP) located on the island of South Uist in the Outer Hebrides, Scotland (Winston,

215 2004; location indicated in Fig. 1a) provides an overview of the wind conditions during the

216 extended NAWDEX campaign period (10 September – 20 October 2016). The ATRAD STP

217 installed at the site has an operating frequency centered at 64 MHz and is able to provide wind

218 measurements up to an altitude of 20 km with a vertical resolution of 500 m. It runs continuously

219 providing data to European meteorological services through the EUMETNET E-PROFILE

220 Program (http://eumetnet.eu/activities/observations-programme/current-activities/e-profile/).

221 Very high frequency (VHF) radio waves are generated by a 12x12 antenna array. The directional

222 beams are partially scattered off irregularities in the atmospheric refractive index, and the LOS

223 winds are derived from the Doppler-shifted return frequency. Horizontal wind components are

224 constructed from a cyclic sequence of 5 vertical and near-vertical beam pointing directions

225 known as Doppler Beam Swinging. The dwell time for each direction is 1 minute, giving a

226 maximum temporal frequency of 5 minutes, however to reduce measurement errors the data

227 transmitted on the global telecommunication system (GTS) via the E-PROFILE network is

228 averaged over 30 minute periods, and it is this data that is utilized here (data is available for

229 download from the Met Office, 2008). Typical measurement areas at ~10 km altitude are 5x5

230 km. The STP data was assimilated at ECMWF and Met Office.

231   The accuracy of the current configuration of the South Uist wind profiler has not been

232 assessed systematically against independent high resolution observations, however, a number of

233 similar STP systems from the same manufacturer located in Australia have recently been

234 evaluated against collocated radiosonde observations by Dolman and Reid (2018). They find the

235 line of best fit between the individual wind components measured by the two techniques to be in

236 the range 0.93-0.97. Earlier STP systems have been systematically evaluated by Dibbern et al.

237 (2001) who found typical mean wind speed biases relative to radiosonde measurements of order

238 0.09 m s^{-1} with a standard deviation of 1.5 m s^{-1}.

239 *c. Modelled winds*

240   For the comparison, we use ECMWF operational analysis and short-term forecast fields

241 from the atmospheric high resolution model (HRES, IFS cycle 41r2) with spectral truncation

242 TCo1280 (Malardel et al. 2016). The data was retrieved from ECMWF's Meteorological

243 Archival and Retrieval System (MARS) and interpolated to a 0.125°x0.125° longitude-latitude

244 grid (~14 km). The IFS is a hydrostatic atmospheric model that uses a hybrid-pressure vertical

245 coordinate with 137 levels that transition from terrain-following surfaces into pressure surfaces

246 with increasing altitude (Simmons and Burridge 1981). To compare with wind observations, first

247 the pressure at each level is calculated by using the surface pressure before the geopotential

248 height can be derived from integrating the hydrostatic equation using pressure and temperature

249 profiles. Details on the vertical discretization and altitude calculation can be found in the IFS

250 documentation in Part III: Dynamics and Numerical procedures (available at

251 https://www.ecmwf.int/en/forecasts/documentation-and-support). We use 6-h analysis fields

252 (0000, 0600, 1200 1800 UTC) in combination with hourly forecasts initialized from 0000 and

253 1200 UTC for the intermediate time steps (e.g., Schäfler et al. 2010) as higher temporal

254 frequency reduces the error in interpolating model data to observation points. For example, this

255 strategy is used by many authors for air mass trajectory calculations, despite the differences

256 between analyses and short-range forecasts, because the reduced interpolation error has been

257 shown to reduce net trajectory error (e.g., Stohl et al. 2001).

258   The NAWDEX wind observations are also compared with operational analyses and

259 forecasts from the UK Met Office using the Met Office Unified Model (MetUM). The MetUM is

260 a non-hydrostatic fully compressible model with deep atmosphere dynamics. The model version

261 in use in 2016 was the GA6.1/GL6.1 science configuration (Walters et al. 2017) operating with a

262 horizontal N768 grid (approx. 17 km grid-spacing in mid latitudes), with 70 vertical levels on a

263 terrain-following hybrid-height Charney–Phillips grid. Since this model is formulated in hybrid-

264 height coordinates, no vertical integration is required to derive altitude values. To compare with

265 the observations, the wind components are output on model levels and simply interpolated in the

266 horizontal and vertical to the coordinates of the observations using linear interpolation in space

267 and time. Forecasts are initialized from analyses at 6-h intervals (0000, 0600, 1200 and 1800

268 UTC) with data output at 1-h intervals.

269   Please note that the DWL profile data is an independent data set meaning that it was not

270 assimilated by the IFS or MetUM data assimilation systems. In contrast, all dropsondes released

271 during NAWDEX (Schäfler et al. 2018) and the STP data were distributed on the GTS and

272 assimilated in the ECMWF (Schindler et al. 2020) and the Met Office prediction systems.

273   Figure 2 shows the distribution of IFS and MetUM model levels between ground and 15

274 km altitude in comparison with the vertically constant resolution of 100 m for the DWL and 500

275 m for the STP at South Uist. In the region 8 - 14 km where the jet stream is typically observed,

276 the IFS provides 19 vertical levels with a mean vertical distance of ~300 m ranging from 290 m

277 to 310 m. The MetUM provides 11 levels at a mean vertical separation of ~550 m ranging from

278 460 m to 630 m in this region. As we are interested in the model capability to capture the

279 observed sharp gradients at the tropopause, we perform the comparisons at the vertical resolution

280 of the DWL and by linearly interpolating the model data in the vertical to the observation

281 location. Likewise, the 1-hourly model data is bi-linearly interpolated in the horizontal to the

282 profile location and linearly in time to the observation time (Schäfler et al. 2010). Please note

283 that for the dropsondes, the model data was interpolated to the location along the fall trajectory

284 of each dropsonde (tracked by GPS). In case of the wind profiler we used data at a 6-hourly time

285 resolution and only compare profiles at the time of the analysis to avoid an influence of short-

286 term forecast error.

287 **3. Case Study**

288 *a. Synoptic overview*

289 First, a case study on NAWDEX Intensive Observation Period (IOP) 3 on 23 September

290 2016 is presented that comprises HALO (RF 03), DLR Falcon (RF 04) and the FAAM Bae 146

291 (RF 01) flights that observed ascending air masses within cyclone Vladiana (Schäfler et al.

292 2018). In this paper the focus is on the flight of the DLR Falcon southeast of Iceland between

293 0710 UTC and 1017 UTC (Fig. 3) that was coordinated with HALO between 0800 UTC and

294 0900 UTC. After the joint leg, the DLR Falcon returned to Keflavik and HALO turned

295 southwestward to observe a strong warm conveyor belt (WCB) related to cyclone Vladiana

296 (Oertel et al. 2019). At 0900 UTC the center of cyclone Vladiana (V) was located south of

297 Iceland and a second low to the west (Fig. 3a). The occluded frontal system related to Vladiana

298 is visible in the increased relative humidity at 700 hPa north and west of the cyclone center and

299 in the clouds along the cold and warm fronts in the eastern and south-eastern sector of the

300 cyclone. In the upper-level outflow of the WCB, which can be seen from the approaching high-

301 level clouds (Fig. 4), a weak ridge has formed with its axis from northwestern Scotland towards

302 Iceland (Fig. 3b). On their coordinated leg, the DLR Falcon and HALO entered a region of

303 increased jet stream winds along the northeast flank of the ridge (Fig. 3b). Increased jet stream

304 winds follow the 2 PVU contour on the 320 K isentropic surface (compare Figs. 3a and 3b) and a

305 second wind speed maximum occurred along the western flank of the ridge. On the coordinated

306 leg dropsonde observations were made by the HALO aircraft (see colored dots in Fig 3b). The

307 aircraft were separated by only 50-km horizontal distance along the coordinated flight leg.

308 Additionally, the flight was located relatively close to the wind profiler in South Uist, Scotland

309 (Fig. 3b) that was observing the jet stream while it moved over the station.

310 *b. Observations and model evaluation*

311   Figure 5a shows DWL wind speed observations along the entire 2340 km long flight

312 between 0710 UTC and 1017 UTC (see track in Fig. 3a). After take-off at Keflavik, the Falcon

313 initially loitered near Iceland between 0710 UTC and 0800 UTC to wait for the HALO aircraft to

314 join the coordinated flight leg between 0800 UTC and 0900 UTC towards the southeast and after

315 that returned along the same track to Iceland. In the first part of the flight leg, the data coverage

316 in clean and dry air is low and restricted to a band extending from 1000 m to about 1500 m

317 beneath the aircraft and to the lowest ~2 km above the ocean. In the upper band, the signal

318 intensity is high near the aircraft whereas an increased load of sea salt aerosol and low-level

319 clouds increases the atmospheric return near the surface (c.f. low level clouds northeast of the

320 WCB-induced cirrus in Fig. 4). The data coverage improves and the observed wind speeds

321 increase up to a maximum of 58 m s^{-1} when both aircraft approached the upper-level cirrus

322 clouds at about 0825 UTC and entered the region of the jet stream. The return along the same

323 flight track causes the symmetry in the wind field in Fig. 5a. The following discussion

324 concentrates on the coordinated part and the return flight with increased upper-level winds

325 between 5 km and 12 km altitude (grey box in Fig. 5a). The DWL observations in this subset and

326 the complementary in situ and dropsonde observations (Fig. 5b) depict the jet stream. Dropsonde

327 winds above and below the DWL observations confirm that, despite the limited data coverage,

328 the DWL captured the entire vertical extent of the jet stream. Maximum wind speeds follow the

329 dynamical tropopause with increased static stability above, as visible from the large vertical

330 gradient of potential temperature. In the following we use the term tropopause as a synonym for

331 the dynamical tropopause, where PV equals 2 PVU. North of cyclone Vladiana, a colder Arctic

332 air mass was advected beneath the ascending warm air and formed a tropopause fold structure

333 along the transect that was also intersected on the return flight. The ascending warm air mass

334 with elevated tropopause altitude can be characterized by two separate regions. The first part

335 with tropopause altitudes of about 9 km (~0812-0826 UTC and 0948-1000 UTC) features low

336 data coverage in the tropospheric air mass indicating a lack of cirrus clouds, while the second

337 region with the tropopause located at about 10 km altitude (~0826-0948 UTC) is characterized

338 by increased returns from the DWL due to the cirrus clouds.

339   Figures 5c and 5d show differences of horizontal wind speed between ECMWF IFS and

340 Met Office MetUM forecasts (using +8h, +9h and +10h forecasts for the IFS and +2h, +3h and

341 +4h for the MetUM) and DWL observations, respectively. The IFS shows coherent areas of

342 increased negative wind speed differences above and below the tropopause corresponding to

343 underestimated winds with peak values of up to -17 m s^{-1}. The MetUM wind speed differences

344 are slightly weaker and feature positive and negative regions that range between -10.5 m s^{-1} and

345 9.5 m s^{-1}. Please note that the depicted error structures are mirrored on the return flight towards

346 Iceland. The consistency of the wind speed differences derived from the three measurement

347 types; DWL, in situ and dropsondes, underlines the reproducibility and representativeness of the

348 measurements. The dropsonde profiles suggest that largest differences occurred near the

349 tropopause. The IFS and MetUM wind speed differences differ substantially, although, it can be

350 noted that the most negative differences in the MetUM tend to occur at approximately the same

351 location as in the IFS. Interestingly, the IFS and MetUM tropopause altitude is different as can

352 be seen from the PV distribution in Fig. 6. The tropopause fold and leading edge of the

353 tropospheric air mass appear earlier along the section in the MetUM which corresponds to a

354 northwestward shift. Similarly, the second increase in tropopause altitude, i.e. the region of low

355 PV values that was approached at about 0820 UTC in the MetUM (Fig. 6a) and is located further

356 northwest along the flight track than in the IFS (Fig. 6b). Towards the southeast of the flight

357 section MetUM overestimates the jet stream wind (Fig. 5d), most likely caused by a different

358 representation between the models of the dynamics associated with the WCB outflow of

359 Vladiana, that is suggested by the higher diagnosed tropopause in the MetUM compared to the

360 IFS in this region. Although this indicates the importance of a correct representation of the

361 tropopause altitude, a vertical shift would be expected to show up as a vertical dipole-like

362 structure in the wind speed differences, while this is not the structure found.

363   To investigate the representation of winds near the tropopause in more detail, observed and

364 modelled wind profiles at the location of the six dropsondes are examined (Fig. 7). The close

365 correspondence of DWL measurements (dots) and dropsonde winds (colour lines) for these six

366 profiles, is consistent with the general statistical comparison shown in Fig. 1c. The maximum

367 wind speed was observed by the DWL at the location of the easternmost dropsonde with 57.5 m

368 s^{-1} at 10.1 km altitude. Unfortunately, the associated dropsonde was launched at a lower altitude

369 of 8.6 km (after HALO descended to a lower flight level) and therefore did not capture this wind

370 maximum (Fig. 5b). A qualitative comparison of the observations (Fig. 7a) and the IFS profiles

371 interpolated to the observation points (Fig. 7b) shows that the altitude of the wind maxima

372 coincides well, while both the strength of the wind maximum and the vertical gradients are

373 underestimated resulting in increased negative wind speed differences in the jet stream above 9

374 km (Fig. 7c). The observations exhibit a step-like change in vertical wind shear at ~10 km

375 altitude, which is not represented in the IFS. The MetUM forecasts (Fig. 7e) show a more

376 realistic representation of the peak wind speeds. However, the strong vertical gradients are

377 underestimated especially above the wind maximum where the observed step-like change in

378 wind speed with height is not represented correctly which results in increased wind speed

379 differences (Fig. 7f).

380   To account for the variability in tropopause altitude along the flight and the height of the

381 wind maximum that differs between the dropsonde locations, wind speeds are displayed with

382 respect to their vertical distance to the tropopause identified by 2 PVU (Figs. 7g-l). Using the

383 tropopause as a reference is an established approach to investigate tropopause sharpness and

384 related trace chemical gradients (e.g., Birner 2006, Pan et al. 2004). In tropopause-relative

385 coordinates, the observed wind profiles transecting the jet stream (sondes 2 to 6) collapse on

386 each other showing that the observed peak wind speed and abrupt change in vertical wind shear

387 is approximately co-located with the dynamic tropopause defined in terms of simulated PV.

388 However, there are differences using the tropopause of the IFS (Fig. 7g) and the MetUM (Fig.

389 7j). For example, the maximum wind in DWL observations at the easternmost dropsonde profile

390 (dots in Fig. 7g) is situated less than 300 m above the IFS tropopause, while the MetUM

391 tropopause is only 100 m above this DWL wind maximum (Fig. 7j). These displacements are

392 less than the model level spacing in the IFS and MetUM and therefore better correspondence

393 cannot be expected. Although the tropopause location has some inherent uncertainty, difference

394   features from multiple profiles are more coherent in the tropopause-relative framework. The

395   distributions of modelled wind speeds (Figs. 7h and k) and respective differences (Figs. 7i and l)

396   emphasize the finding that the IFS underestimates the wind maxima and tropopause sharpness

397   and that the MetUM performs better in terms of wind speeds and gradients in this particular case.

398   Note also that the observations are compared with longer lead time forecasts for the IFS than for

399   the MetUM (due to the operational forecast frequency). Nevertheless, this analysis shows that

400   the wind speed differences are influenced by diverse uncertainties related to the representation of

401   the peak winds, the strength of vertical wind shear on the stratospheric and tropospheric sides of

402   the tropopause and uncertainty in tropopause altitude.

403   Figure 7 shows that the vertical gradient of wind speed is under-represented on both sides

404   of the tropopause over a considerable distance (more than a km), which spans several model

405   levels in both the IFS and MetUM. To further investigate the structure of vertical wind shear,

406   Figure 8a shows the magnitude of the vertical shear in the vector wind, calculated at points along

407   the cross section, as derived from the DWL and dropsonde observations. Thin, but horizontally

408   extended, layers of high vertical wind shear are observed along the tropopause and also ~1 km

409   above it. Although each layer is too thin to be resolved in the NWP data (Fig. 8 b and c), both

410   models indicate increased vertical shear above the tropopause. The important question for

411   Rossby wave propagation is whether the vertical wind shear above and below the tropopause is

412   too weak in the models on average, since this would imply a weaker PV gradient.

413   For a quantitative comparison, Fig. 9 shows horizontal averages of wind speeds and vertical

414   shear in a tropopause-relative framework for this flight. Figure 9a and 9b reiterate the finding of

415   increased wind errors above the tropopause in the IFS compared to MetUM (see also from Fig.

416   5c and d). Vertical wind shear is higher on the stratospheric side of the tropopause in both

417   models (Fig. 9 c and d), however, clearly underestimated compared to the observations. The

418   higher spread in the observed vertical shear is dominated by the small-scale layers (Fig. 8a) that

419   cannot be represented at the current model resolution. The maximum observed vertical shear by

420   the DWL with a 100-m vertical resolution is 0.23 s^{-1}, which certainly is a local extreme. For this

421   case study, the median observed vertical shear is 0.031 s^{-1} above and 0.013 s^{-1} below the

422   tropopause. Corresponding median values are 0.018 s^{-1}/0.010 s^{-1} for the IFS and 0.021 s^{-1}/0.013 s^{-}

423   ^{1} for the MetUM which indicates a significant underestimation of shear, especially above the

424   tropopause, in this case.

4. Statistical assessment of wind speed differences

426   Section 3 focused on the structure of the observed wind speeds and vertical shear for one

427   case study and gave an indication of significant uncertainties in the representation of jet stream

428   winds in global NWP models, especially at the level of the mid-latitude tropopause. To

429   investigate whether these uncertainties were systematically occurring features during NAWDEX,

430   the following section addresses campaign statistics based on the entire DWL data set and the

431   wind profiler data at South Uist (location in Fig.1).

a. Wind lidar data set

433   Frequency distributions for all DWL wind speed observations from NAWDEX in

434   tropopause-relative coordinates make use of the IFS definition of the tropopause in Fig. 10a and

435   the MetUM tropopause in Fig. 10b. Both wind distribution and mean and median wind curves

436   look similar. Small differences between both can be explained by slightly variable tropopause

437   altitudes as discussed in section 3b. The highest average winds peak around the tropopause with

438   a maximum median (mean) wind speed of ~41 m s^{-1} (~38 m s^{-1}) which is found in the 500 meters

439   below the tropopause. Above and below the tropopause, winds quickly decline. The altitude

440   range from 1 km above to 2 km below the tropopause provides slightly weaker maxima in the

441   frequency distributions indicating broader distributions and thus more variability in the winds.

442   The highest data coverage from the DWL is found around the tropopause, which is a result from

443   the chosen flight altitude. Some increased frequencies above the tropopause appear at high wind

444   speeds and are related to situations where the tropopause altitude rapidly decreases in the

445   stratospheric air, i.e. on the cyclonic shear side of the jet stream, for example at ~0810 UTC in

446   Fig. 5b. In such situations high wind speeds are attributed to low tropopause altitudes.

447   The median (mean) wind speed difference of -0.41 m s^{-1} (-0.68 m s^{-1}) for the IFS and -0.15

448   m s^{-1} (-0.28 m s^{-1}) for the MetUM derived from the 77541 modelled and observed wind speeds is

449   small. Frequency distributions of the differences for 1 km altitude bins relative to the tropopause

450   provide information on the vertical distribution of biases in the IFS (Fig. 10c) and MetUM (Fig.

451   10d). Generally, the median (mean) differences are small at all altitudes ranging between -1.54 m

452   s^{-1} (-1.72 m s^{-1}) and 0.38 m s^{-1} (0.30 m s^{-1}) in the IFS, and -0.9 m s^{-1} (-1.0 m s^{-1}) and 0.36 m s^{-1}

453   (0.22 m s^{-1}) in the MetUM. Please note that most of the wind speed differences are found to be

454   statistically significant based on the 95% confidence interval that was calculated from 1000

455   bootstrap samples. Interestingly, the highest variability in the differences is visible in the altitude

456   bin directly above the tropopause in both models indicating increased uncertainty in the

457   representation of the winds at this location. This is particularly striking when viewing individual

458   frequency curves for each range bin (Fig. 11). The differences in the first kilometer above the

459   tropopause provide a significantly broader distribution (standard deviation of 3.98 m s^{-1} for the

460   IFS and 3.82 m s^{-1} for the MetUM) compared to the mean curve (standard deviation of 3.23 m s^{-1}

461   for the IFS and 3.17 m s^{-1} for the MetUM).

462   Figure 10e, f show the magnitude of vertical shear for the DWL data set. The vertical

463   distribution of median and mean vertical shear using IFS and MetUM is remarkably similar

464   around the tropopause. Observed median (mean) values in the troposphere range from 0.01 s^{-1}

465   (0.013 s^{-1}) to 0.016 s^{-1} (0.02 s^{-1}) with values decreasing with height towards the tropopause.

466   Above the tropopause vertical shear values jump up to values of 0.021 s^{-1} (0.023 s^{-1}) before they

467   again decrease to ~0.014 s^{-1} (0.017 s^{-1}). The increased difference between mean and median

468   levels relates to the skewed distributions at all altitudes. The vertical shear difference to the

469   DWL observations of the IFS (Fig. 10 g) and the MetUM (Fig. 10 h) show an underestimation at

470   all levels with the smallest errors in the 2 km below the tropopause. This is in agreement with the

471   case study presented in Fig. 9. Expressed as a ratio of observed and modelled vertical shear, the

472   factor of underestimation ranges between 1.3 and 5 for the median in both models. The

473   underestimation is lower (factor 1.5 to 2) in the upper troposphere where observed vertical shear

474   is small and directly above the tropopause where the simulated vertical shear shows a maximum

475   (c.f. Fig. 10 e, f).

476   One could ask to what extent this result is reproducible in a different year or season.

477   Therefore, we repeated the statistical comparison for the WindVAL-I campaign that was

478   conducted from Iceland in the period 11 to 29 May 2015 and that used the same DWL

479   instrument to measure horizontal wind speed (Reitebuch et al. 2017; Marksteiner et al. 2018).

480   Fig. A1a shows again increased data coverage around the tropopause. Although the mean winds

481   are smaller than during NAWDEX and almost constant with altitude for this campaign (Fig.

482   A1a), again the largest variability in the wind speed differences occurs in the altitude bin directly

483   above the tropopause (Fig. A1b). Vertical wind shear (Fig. A1c) also shows a comparable

484   distribution with weakest differences in the upper troposphere. As during NAWDEX, the vertical

485 shear in the IFS (Fig. A1d) is too weak at all altitudes with underestimation ratios ranging

486 between 2 and 3.5 being higher in the lower troposphere.

487 *b. Ground-based wind profiler data set*

488 To investigate the representativeness of the DWL comparison with NWP data, the

489 ECMWF and Met Office analysis data are additionally compared with STP wind profiles at

490 South Uist providing a continuous time series in the NAWDEX observation area. During the

491 NAWDEX period the wind situation above South Uist is characterized by large variability (Fig.

492 12a). Especially in the first half of the period, repeated passages of strong wind events

493 accompanied by increased tropopause variability are noticeable. The tropopause location in

494 MetUM and IFS are located at similar altitudes with a mean difference of approximately 100 m.

495 Jet stream observations are related to IOP 1 (tropical cyclone Ian) on 17 September, IOP 2

496 (cyclone Ursula) on 22 September, IOP 3 (Vladiana) from 23 to 25 September and IOP 4

497 (tropical storm Karl) from 27 to 29 September. Increased winds on 3 and 7 October can be

498 related to IOP 6 (the Stalactite Cyclone) and IOP 8, respectively. In the second half of the time

499 series, upper-level wind speeds, as well as the variability of the tropopause, become lower as a

500 block established over Europe (Schäfler et al. 2018).

501 Figure 12b shows 6-h forecasts from the Met Office which correspond to the background

502 forecasts in the data assimilation process. In the one-month period, two obvious situations appear

503 that feature increased wind speed differences. First, frontal passages, which can be identified

504 from tilted isentropes, most often feature overestimated wind speeds in the lower troposphere.

505 Second, situations with strong upper-level winds, elevated tropopause altitudes and sharp vertical

506 gradients in winds and static stability predominantly feature underestimated wind speeds in the

507 first 2 km above the tropopause. Figure 12c shows the Met Office analysis profiles compared

508 with the STP observations. Obviously the data assimilation of the STP observations reduces the

509 errors in the background field. However, negative analysis differences remain in situations of

510 increased errors in the 6h forecast, e.g. on 12, 17 and 24-25 September. The comparison of

511 ECMWF analysis profiles with the STP observations (Fig. 12c) reveals very similar errors, even

512 in situations of large tropopause variability, which is remarkable as both forecasting systems use

513 different data assimilation schemes and models. Consistent with the DWL observations, the

514 diagnosed wind speed errors show increased uncertainty of the winds above the tropopause with

515 a tendency of an underestimation, especially above tropopause ridges.

516 **5. Conclusions**

517   A unique set of comprehensive airborne and ground-based wind profile observations was

518 used to characterize the structure of the jet stream and to evaluate the representation of winds

519 across the tropopause in the two state-of-the-art global operational NWP forecasting systems of

520 the ECMWF and the Met Office. The study covers the high latitude North Atlantic Ocean where

521 the availability of conventional data sources for winds are sparse. The NAWDEX period was

522 characterized by high wave activity and variable predictability (Schäfler et al. 2018).

523   The independent (not assimilated) DWL data set features 1922 wind profiles at high

524 horizontal (8.6 km profile spacing) and vertical resolution (100 m) during 8 flights. Comparison

525 of DWL wind profiles with dropsondes demonstrates the low measurement error, which is

526 needed to quantify meteorological analysis errors. Although NWP models are characterized by

527 lower horizontal and vertical resolution, compared to the DWL data, the average representation

528 of the winds is remarkably good. Statistical assessment using the DWL data set provided median

529 (mean) biases of -0.41 m s^{-1} (-0.68 m s^{-1}) for the IFS and -0.15 m s^{-1} (-0.28 m s^{-1}) for the MetUM.

530 The comparison with temporally continuous lidar profiles requires a temporal interpolation from

531 NWP analysis and forecast data, so it is likely that forecast errors may have affected the

532 differences with NWP data. The longer forecast intervals that were used for the ECMWF data

533 (forecasts initialized at 0000 and 1200 UTC) compared to the MetUM (initialized at 0000, 0600,

534 1200 and 1800 UTC) may have caused slightly higher average negative wind speed differences

535 in the IFS. NWP profiles were found to be smoother and less detailed for the IFS compared to

536 the MetUM. Diagnosed average biases are smaller at all altitudes relative to the early 2000s that

537 were characterized by biases in the order of 5-10 % (Tenenbaum 1991, 1996; Rickard et al.

538 2001; Cardinali et al. 2003). This study corroborates that recent advances in NWP connected to

539 improved data assimilation methods, improved data quality and availability, as well as increased

540 model resolution and better formulation, have led to a significant improvement of the wind

541 analysis quality in the mid-latitudes. However, Horányi et al. (2015) have shown that already

542 small scale systematic observational wind errors in the order of 1 m s^{-1} are able to significantly

543 deteriorate forecast quality after 24 h.

544   This study also shows that wind errors still reach values exceeding ±10 m s^{-1} (i.e. about 3σ

545 of the difference distributions) for individual cases and that error structures are of large extent

546 and spatially correlated (up to ~500 km in the horizontal and 1-2 km in the vertical) in the

547 analyses and short-range forecasts of ECMWF and Met Office. DWL measurement errors are

548 found to be smaller than the errors in NWP data and typically uncorrelated. Forecast and analysis

549 error structures are most prominent immediately above the tropopause on the flanks of upper-

550 level ridges where strongest vertical wind-shear occurs (e.g., Fig. 5). The same wind error

551 structures are found in the comparison of modelled profiles with the STP radar profiler data over

552 a 6-week period (Fig. 12). The spatial structure of near-tropopause errors is similar in ECMWF

553 and Met Office short-range forecasts and analyses, even though the forecast models and data

554 assimilation schemes differ greatly. Moreover, increased wind uncertainty directly above the

555 tropopause could be confirmed for the WindVAL-I campaign in 2015.

556   The different observation types, used in this study, have very different sampling

557 characteristics. The DWL observations represent samples from 8.6 km line segments, the STP

558 profiler measurements represent a volume of size 5 km x 5 km x 500 m (at 10 km) averaged over

559 30 minutes, while the dropsondes are effectively point measurements along the sonde trajectory.

560 These are compared with winds from NWP models represented on a grid with an approximate

561 horizontal spacing of 15 km and vertical level spacing of 300 m in the IFS, 17 km and 550 m in

562 the MetUM (see Fig. 2). Therefore, such a validation of NWP data will inevitably be affected by

563 a representation (sampling) error (e.g. Janjić et al. 2017). For this reason, data assimilation uses

564 an assigned observation error that is a combination of instrument and representation error.

565 Weissmann et al. (2005) estimate the representation error to range between 1.5 m s^{-1} for a point

566 measurement in a 40 km grid box and 0.15 m s^{-1} for a line measurement through that box. They

567 argue that typical assigned observation errors of 2-3 m/s may be too high. To account for the

568 difference in the representation of the data, the observations could be averaged before

569 comparing. However, this study aimed at investigating how far the models deviate from "nature"

570 as observed by the DWL and STP. The large horizontal and vertical scales of the correlated wind

571 error structures (several hundred km horizontally and 1-2 km vertically) can be represented on

572 the grids used by the NWP models. Furthermore, error features persisted for extended periods of

573 time (hours to several days) in the time-series of the STP (Fig. 12). The magnitude of the errors

574 (up to 10 m s^{-1}) and the systematic occurrence at the flank of and above ridges indicates that

575 these structures cannot be explained by representation and measurement error alone.

576   The analysis of vertical wind shear revealed that observed values rapidly increase above the

577   tropopause and that median vertical shear is underestimated in both models at all altitudes by a

578   factor of 1.5 to 5. This is line with Houchi et al. (2010) who found an underestimation by a factor

579   of 2.5 to 3 for vertical shear of the zonal and meridional wind and illustrate that most of the

580   missing vertical shear can be explained by the lower vertical resolution of the model profiles. By

581   vertically averaging winds they estimate an effective vertical resolution for wind shear of 1.7 km

582   for the IFS version in 2006 with 91 model levels. Furthermore, the missing small-scale

583   variability of vertical wind shear that was demonstrated along the DWL cross section (Fig. 8) is

584   in line with their findings.

585   **6. Implications of the findings**

586   Underestimation of vertical shear by models has implications locally for the nature and

587   intensity of turbulence and the parametrization of subgrid-scale processes (Houchi et al. 2010).

588   For example, by changing the bulk Richardson number used in parametrization. In addition, the

589   under-estimation of the change in vertical shear across the tropopause that has been discovered

590   here has a non-local, large-scale consequence: the dynamics of Rossby wave propagation depend

591   on the meridional gradient in the PV distribution which is dominated by the change in vertical

592   shear. Direct calculation of Ertel PV and its gradient across the jet stream from observations

593   requires measurements of horizontal wind and temperature with high resolution in both the

594   vertical and horizontal. This is very difficult to achieve, although Harvey et al. (2020) present an

595   example from a high density dropsonde section crossing the jet stream in NAWDEX IOP4.

596   However, the meridional gradient in quasi-geostrophic PV, q, across a zonal flow, u (see Hoskins

597   and James, 2014) can be estimated using the DWL wind data (without coincident high resolution

598   temperature profile data):

26

$$\frac{\partial q}{\partial y} = \beta - \frac{\partial^2 u}{\partial y^2} - \frac{1}{\rho_R}\frac{\partial}{\partial z}\left(\rho_R \frac{f^2}{N^2}\frac{\partial u}{\partial z}\right) \approx \beta - \frac{2(u_e - u_J)}{L^2} - \frac{f^2}{\Delta z}\left(\frac{\Lambda_s}{N_s^2} - \frac{\Lambda_t}{N_t^2}\right)$$

599 where $\rho_R(z)$ is a reference density profile (assumed to vary less quickly with z than u(z) to

600 derive the right side approximation), f is Coriolis parameter, β is its meridional gradient, N_t and

601 N_s are the Brunt-Vaisala frequencies for troposphere and stratosphere and Λ_t and Λ_s are the

602 respective vertical wind shears separated by a specified distance Δz across the tropopause zone.

603 The horizontal curvature term is estimated by centred difference over cross-jet scale, L, where u_J

604 represents the jet core speed and u_e is the environmental wind speed at distance L from the core.

605 At 62 N, $f = 1.3$ x 10^{-4} s^{-1} and $\beta = 1.1$ x 10^{-11} m^{-1} s^{-1}. Using numbers from the observed cross-

606 section Fig. 5b, it is estimated that the meridional wind curvature term is approximately $8\text{-}12\beta$

607 (using $L=600$ km, $u_J=50$ m s^{-1} and $u_e = 30$ m s^{-1}) and the vertical wind curvature term is as much

608 as $2000\text{-}2500\beta$ (using Δz of 100 m, $N_s = 2$ x 10^{-2} s^{-1}, $N_t = 10^{-2}$ s^{-1}, $\Lambda_s = $ -3 x 10^{-2} s^{-1} , $\Lambda_s = 10^{-2}$ s^{-1})

609 illustrating how dominant the change in vertical wind shear is in the estimate of meridional PV

610 gradient in the regions where errors are observed. If the same change in vertical shear in the

611 model is spread over 1 km (compare profiles in observations and analyses in Fig. 7) then this

612 term would be 10 times smaller in the model (although still dominant).

613 Background forecasts (+6h) for the atmospheric column above the STP profiler at South

614 Uist showed similar wind error structures above the tropopause with higher amplitude than seen

615 in the analyses. This indicates that data assimilation reduces the background forecast model error

616 but cannot eliminate it. Future work is needed to evaluate whether assimilated wind profiles tend

617 to improve near-tropopause wind fields through sharpening the gradients. Pilch Kedzierski et al.

618 (2016) found that static stability increments tend to strengthen the tropopause gradients.

619 Schindler et al. (2020) demonstrate an overall positive impact of additional wind information

620 from NAWDEX radiosonde and dropsonde observations on the mid-tropospheric flow.

621   Additional research is needed to quantify errors of other quantities across the tropopause

622   and how these uncertainties relate to our findings. Pilch Kedzierski et al. (2016) indicate an

623   excessively diffuse tropopause in terms of temperature gradients as verified by radio-occultation

624   observations. Another important quantity is water vapor providing a tropopause-based step

625   change in concentration. The resulting sharp peak in longwave radiative cooling at the

626   tropopause is able to strengthen the positive Ertel PV anomaly above, and negative PV anomaly

627   below, the tropopause (Chagnon et al. 2013, Spreitzer et al. 2019) thus increasing tropopause

628   sharpness (Ferreira et al. 2015). Saffin et al. (2017) used the MetUM with PV tracers that

629   diabatic processes, including longwave cooling, microphysics and the turbulent mixing

630   parametrization all act to increase the tropopause PV contrast while the non-conservative

631   numerical effects associated with the dynamical core of the model compete, acting to reduce the

632   PV contrast. In forecasts, the PV anomalies associated with these tendencies saturate in about 24

633   hours indicating that the model has found its own climatological balance of processes at the

634   tropopause. However, the true balance affecting tropopause structure in the atmosphere, where

635   numerical effects are absent and the tropopause is typically much sharper, is not known.

636   Furthermore, the NAWDEX observations show that a major increase in model vertical resolution

637   near the tropopause (by at least a factor of 3) would be required to resolve the abrupt change in

638   both vertical wind shear and static stability there, indicating scope to increase forecast skill

639   through better representation of the tropopause and its influence on the propagation of Rossby

640   waves.

641   In August 2018 the European Space Agency (ESA) Aeolus satellite mission was launched,

642   carrying the first wind lidar in space. It is expected to contribute significantly to improved

643   representation of the winds in global analyses and forecasts (e.g., Stoffelen et al. 2005; ESA

644   2008; Reitebuch 2012). It will be interesting to evaluate to what extent a large number of

645   observations from Aeolus in oceanic regions with hitherto sparse wind data coverage will impact

646   winds in the mid-latitudes and more specifically at the tropopause.

663   **Appendix**

664   In 2015, the WindVAL-I campaign was conducted from Iceland using the same set of

665   instruments on-board the Falcon. Unlike NAWDEX, this campaign focused rather on the

666   preparation of the Aeolus calibration and validation in various wind and cloud scenes than on

667　specifically observing jet stream situation (Reitebuch et al. 2017). Figure A1 shows all 141906

668　DWL wind observations in tropopause-relative coordinates that were measured from 14 research

669　flights in the surrounding of Iceland.

670　**References**

671　Baker, W. E., and Coauthors, 2014: Lidar-Measured Wind Profiles: The Missing Link in the
672　　　Global Observing System. *Bull. Amer. Meteor. Soc.*, **95 (4)**, 543–564, doi:10.1175/BAMS-
673　　　D-12-00164.1.

674　Baumgart, M., M. Riemer, V. Wirth, F. Teubler, and S.T. Lang, 2018: Potential Vorticity
675　　　Dynamics of Forecast Errors: A Quantitative Case Study. *Mon. Wea. Rev.,* **146**, 1405–1425,
676　　　https://doi.org/10.1175/MWR-D-17-0196.1

677　Belmonte Rivas, M. and A. Stoffelen, 2019: Characterizing ERA-Interim and ERA5 surface
678　　　wind biases using ASCAT, *Ocean Science*, **15 (3)**, 831--852, doi:10.5194/os-15-831-2019

679　Birner, T., 2006: Fine-scale structure of the extratropical tropopause region. *J. Geophys. Res.:*
680　　　*Atmospheres*, **111 (D4)**, doi:10.1029/2005JD006301.

681　Cardinali, C., L. Rukhovets, and J. Tenenbaum, 2004: Jet Stream Analysis and Forecast Errors
682　　　Using GADS Aircraft Observations in the DAO, ECMWF, and NCEP Models. *Mon. Wea.*
683　　　*Rev.*, **132 (3)**, 764–779, doi:10.1175/1520-0493(2004)132<0764:JSAAFE>2.0.CO;2.

684　Chagnon, J., S. Gray, and J. Methven, 2013: Diabatic processes modifying potential vorticity in a
685　　　North Atlantic cyclone. *Quart. J. Roy. Meteor. Soc.,* **139**(674), 1270–1282.
686　　　doi:10.1002/qj.2037

687　Chouza, F., O. Reitebuch, A. Benedetti, and B. Weinzierl, 2016: Saharan dust long-range
688　　　transport across the Atlantic studied by an airborne Doppler wind lidar and the MACC
689　　　model. *Atmos. Chem. Phys.*, **16 (18)**, 11 581–11 600, doi:10.5194/acp-16-11581-2016.

690　Davies, H.C. and M. Didone, 2013: Diagnosis and Dynamics of Forecast Error Growth. *Mon.*
691　　　*Wea. Rev.,* **141**, 2483–2501, https://doi.org/10.1175/MWR-D-12-00242.1

692　Dibbern, J., W. Monna, J. Nash, and G. Peters, 2001: COST Action 76 - final report.
693　　　Development of VHF/UHF wind profilers and vertical sounders for use in European
694　　　observing systems. *European Commission*.

695　Dolman, B. K., I. M. Reid, and C. Tingwell, 2018: Stratospheric tropospheric wind profiling
696　　　radars in the Australian network. *Earth, Planets and Space*, **70**: 170, doi:10.1186/s40623-
697　　　018-0944-z

698　ESA, 2008: ADM-Aeolus Science Report. *SP-1311* ed., URL:
699　　　http://esamultimedia.esa.int/docs/EarthObservation/SP-1311ADM-Aeolus_Final.pdf

Ferreira, A. P., J. M. Castanheira, and L. Gimeno, 2015: Water vapour stratification and dynamical warming behind the sharpness of the Earth's midlatitude tropopause. *Quart. J. Roy. Meteor. Soc.,* **142**(695), 957–970. doi:10.1002/qj.2697

Gray, S., C. Dunning, J. Methven, G. Masato, and J. Chagnon, 2014: Systematic model forecast error in Rossby wave structure. *Geophys. Res. Lett.*, **41 (8)**, 2979–2987, doi:10.1002/2014GL059282

Harvey, B., J. Methven, and M. Ambaum, 2016: Rossby wave propagation on potential vorticity fronts with finite width. *J. Fluid Mech.*, **794**, 775–797, https://doi.org/10.1017/jfm.2016.180.

Harvey, B., J. Methven, and M.H. Ambaum, 2018: An Adiabatic Mechanism for the Reduction of Jet Meander Amplitude by Potential Vorticity Filamentation. *J. Atmos. Sci.,* **75**, 4091–4106, https://doi.org/10.1175/JAS-D-18-0136.1

Harvey, B., J. Methven, C. Sanchez, A. Schäfler, 2020: Diabatic generation of negative potential vorticity in the North Atlantic and its impact on the jet stream. *Q. J. R. Meteorol. Soc.,* 1-22, doi:10.1002/qj.3747

Hock, T. F., and J. L. Franklin, 1999: The NCAR GPS Dropwindsonde. *Bull. Amer. Meteor. Soc.*, **80 (3)**, 407–420, doi:10.1175/1520-0477(1999)080*h*0407:TNGD*i*2.0. CO;2.

Horányi, A., C. Cardinali, M. Rennie, and L. Isaksen, 2015: The assimilation of horizontal line-of-sight wind information into the ECMWF data assimilation and forecasting system. Part II: The impact of degraded wind observations. *Quart. J. Roy. Meteor. Soc.*, **141,** 1233-1243, doi:10.1002/qj.2551

Hoskins, B.J. and T. Ambrizzi, 1993: Rossby Wave Propagation on a Realistic Longitudinally Varying Flow. *J. Atmos. Sci.,* **50**, 1661–1671, https://doi.org/10.1175/1520-0469(1993)050<1661:RWPOAR>2.0.CO;2

Hoskins, B., and I. N. James, 2014: Rotation in the atmosphere. *Fluid Dynamics of the Midlatitude Atmosphere*, B. J. Hoskins and I. N. James, Eds., John Wiley and Sons, 125–148, https://doi.org/10.1002/9781118526002.ch8.

Houchi, K., A. Stoffelen, G. J. Marseille, and J. De Kloe, 2010: Comparison of wind and wind shear climatologies derived from high-resolution radiosondes and the ECMWF model. *J. Geophys. Res.: Atmospheres*, **115 (D22)**, doi:10.1029/2009JD013196.

Janjić, T., N. Bormann, M. Bocquet, J. A. Carton, S. E. Cohn, S. L. Dance, S. N. Losa, N. K. Nichols, R. Potthast, J. A. Waller, P. Weston, 2017: On the representation error in data assimilation*, Q. J. R. Meteorol. Soc.*, **144**: 1257– 1278. https://doi.org/10.1002/qj.3130

Lux, O., C. Lemmerz, F. Weiler, U. Marksteiner, B. Witschas, S. Rahm, A. Schäfler, and O. Reitebuch, 2018: Airborne wind lidar observations over the North Atlantic in 2016 for the pre-launch validation of the satellite mission Aeolus. *Atmos. Meas. Tech.*, **11 (6)**, 3297–13 3322, doi:10.5194/amt-11-3297-2018.

Malardel, S., N. Wedi, W. Deconinck, M. Diamantakis, C. Kühnlein, G. Mozdzynski, M. Hamrud, and P. Smolarkiewicz, 2016: A new grid for the IFS. ECMWF Newsletter, 146, 23–28.

Marksteiner, U., C. Lemmerz, C., O. Lux, S. Rahm, A. Schäfler, B. Witschas, and O. Reitebuch, 2018: Calibrations and Wind Observations of an Airborne Direct-Detection Wind LiDAR Supporting ESA's Aeolus Mission. *Remote Sens.*, **10(12),** 2056; doi:10.3390/rs10122056

Martius, O., C. Schwierz, and H. Davies, 2010: Tropopause-level waveguide. *J. Atmos. Sci.*, **67 (3)**, 866–879, doi:10.1175/2009JAS2995.1.

Met Office, 2008: Wind Profiler Observations, Part of the Met Office MetDB System. NCAS British Atmospheric Data Centre, https://catalogue.ceda.ac.uk/uuid/9e22544a66ba7aa902ae431b1ed609d6

Oertel, A., M. Boettcher, H. Joos, M. Sprenger, H. Konow, M. Hagen, and H. Wernli, 2019: Convective activity in an extratropical cyclone and its warm conveyor belt - a case study combining observations and a convection-permitting model simulation. *Quart. J. Roy. Meteor Soc.*,**145**, 1406-1426 doi: 10.1002/qj.3500.

Pan, L. L., W. J. Randel, B. L. Gary, M. J. Mahoney, and E. J. Hintsa, 2004: Definitions and sharpness of the extratropical tropopause: A trace gas perspective. *J. Geophys. Res.: Atmospheres*, **109 (D23)**, doi:10.1029/2004JD004982.

Petersen, R. A., 2016: On the Impact and Benefits of AMDAR Observations in Operational Forecasting—Part I: A Review of the Impact of Automated Aircraft Wind and Temperature Reports. *Bull. Amer. Meteor. Soc.*, **97 (4)**, 585–602, doi:10.1175/BAMS-D-14-00055.1

Pilch Kedzierski, R., L. Neef, and K. Matthes, 2016: Tropopause sharpening by data assimilation. *Geophys. Res. Lett.*, **43 (15)**, 8298–8305, doi:10.1002/2016GL069936.

Reitebuch, O., C. Lemmerz, E. Nagel, U. Paffrath, Y. Durand, M. Endemann, F. Fabre, and M. Chaloupy, 2009: The Airborne Demonstrator for the Direct-Detection Doppler Wind Lidar ALADIN on ADM-Aeolus. Part I: Instrument Design and Comparison to Satellite Instrument. *J. Atmos. Oceanic Technol.*, **26**, 2501–2515, doi:10.1175/2009JTECHA1309.1.

Reitebuch, O., 2012: The space-borne wind lidar mission ADM-Aeolus. in Schumann U. (Ed.): Atmospheric Physics – Background, Methods, Trends. Springer Series on Research Topics in Aerospace. ISBN 978-3-642-30182-7, p. 815-827.

Reitebuch, O., C. Lemmerz, O. Lux, U. Marksteiner, B. Witschas, R. R. Neely, 2017: WindVal– Joint DLR-ESA-NASA Wind Validation for Aeolus; Final Report Contract No. 4000114053/15/NL/FF/gp, European Space Agency (ESA), Noordwijk, The Netherlands.

Rickard, G. J., R. W. Lunnon, and J. Tenenbaum, 2001: The Met Office upper air winds: Prediction and verification in the context of commercial aviation data. *Meteor. Appl.*, **8 (3)**, 351–360, doi:10.1017/S1350482701003115.

772 Saffin, L., S. Gray, J. Methven, and K. Williams, 2017: Processes Maintaining Tropopause
773   Sharpness in Numerical Models. *J. Geophy. Res.: Atmospheres*, **122 (18)**, 9611– 9627,
774   doi:10.1002/2017JD026879.

775 Schäfler, A., A. Dörnbrack, C. Kiemle, S. Rahm, and M. Wirth, 2010: Tropospheric Water
776   Vapor Transport as Determined from Airborne Lidar Measurements. *J. Atmos. Oceanic*
777   *Technol.*, **27 (12)**, 2017–2030, doi:10.1175/2010JTECHA1418.1.

778 Schäfler, A., and Coauthors, 2018: The North Atlantic Waveguide and Downstream Impact
779   Experiment. *Bull. Amer. Meteor. Soc.*, **99**, 1607-1637, doi:10.1175/20 BAMS-D-17-0003.1.

780 Schindler, M., M. Weissmann, A. Schäfler, and G. Radnoti, 2020: The impact of dropsonde and
781   extra radiosonde observations during NAWDEX in autumn 2016. *Mon. Wea. Rev.,* **148**,
782   809–824, https://doi.org/10.1175/MWR-D-19-0126.1

783 Schwierz, C., S. Dirren, and H. Davies, 2004: Forced waves on a zonally aligned jet stream. *J.*
784   *Atmos. Sci.*, **61 (1)**, 73–87, doi:10.1175/1520-0469(2004)061h0073: FWOAZAi2.0.CO;2.

785 Simmons, A. J., and D. M. Burridge, 1981: An Energy and Angular-Momentum Conserving
786   Vertical Finite-Difference Scheme and Hybrid Vertical Coordinates. *Mon. Wea. Rev.*, **109**
787   **(4)**, 758–766, doi:10.1175/1520-0493(1981)109h0758:AEAAMCi2.0.CO;2.

788 Spreitzer, E., R. Attinger, M. Boettcher, R. Forbes, H. Wernli, and H. Joos, 2019: Modification
789   of Potential Vorticity near the Tropopause by Nonconservative Processes in the ECMWF
790   Model. *J. Atmos. Sci.*, **76**, 1709-1726, https://doi.org/10.1175/JAS-D-18-0295.1

791 Stoffelen, A., and Coauthors, 2005: The atmospheric dynamics mission for global wind field
792   measurement. *Bull. Amer. Meteor. Soc.*, **86 (1)**, 73–88, doi:10.1175/BAMS-86-1-73.

793 Stohl, A., L. Haimberger, M.P. Scheele, and H. Wernli (2001): An intercomparison of results
794   from three trajectory models. *Meteorol. Applications,* **8**, 127-135.

795 Tenenbaum, J., 1991: Jet Stream Winds: Comparisons of Analyses with Independent Aircraft
796   Data over Southwest Asia. *Wea. Forecasting*, **6 (3)**, 320–336, doi:10.1175/1520-0434(1991)
797   006<0320:JSWCOA>2.0.CO;2.

798 Tenenbaum, J., 1996: Jet Stream Winds: Comparisons of Aircraft Observations with Analyses.
799   *Wea. Forecasting*, **11 (2)**, 188–197, doi:10.1175/1520-0434(1996)011<0188:JSWCOA>
800   2.0.CO;2.

801 UCAR/NCAR - Earth Observing Laboratory. (1993). NCAR Airborne Vertical Atmospheric
802   Profiling System (AVAPS). UCAR/NCAR - Earth Observing Laboratory.
803   https://doi.org/10.5065/D66W9848 Retrieved March 22, 2017/D66W9848

804 Vaisala, 2017: *Drosponde RD94*. URL:
805   https://www.vaisala.com/sites/default/files/documents/RD94-Datasheet-B210936EN-B.pdf.

806 Walters, D., M. Brooks, I. Boutle, T. Melvin, R. Stratton, S. Vosper, H. Wells, K. Williams, N.
807   Wood, T. Allen, and A. Bushell, 2017: The Met Office unified model global atmosphere

808 6.0/6.1 and JULES global land 6.0/6.1 configurations. *Geoscientific Model Development*,
809 **10(4)**, 1487-1520.

810 Wang, J. J., and Coauthors, 2015: A Long-Term, High-Quality, High-Vertical-Resolution GPS
811 Dropsonde Dataset for Hurricane and Other Studies. *Bull. Amer. Meteor. Soc.*, **96 (6)**, 961–
812 973, doi:10.1175/BAMS-D-13-00203.1.

813 Weissmann, M., R. Busen, A. Dörnbrack, S. Rahm, and O. Reitebuch, 2005: Targeted
814 observations with an airborne wind lidar. *J. Atmos. Oceanic Technol.*, **22 (11)**, 1706–1719,
815 doi:10.1175/JTECH1801.1.

816 Winston H., 2004: Vaisala wind profilers support: modernization of upper-air data collection
817 network in the UK. *Vaisala News,* **164**, 24–25

818 Witschas, B., S. Rahm, A. Dörnbrack, J. Wagner, and M. Rapp, 2017: Airborne Wind Lidar
819 Measurements of Vertical and Horizontal Winds for the Investigation of Orographically
820 Induced Gravity Waves. . *J. Atmos. Oceanic Technol.*, **34 (6)**, 1371–1386, doi:10.23
821 1175/JTECH-D-17-0021.1.

822 Witschas, B., C. Lemmerz, A. Geiß, O. Lux, U. Marksteiner, S. Rahm, O. Reitebuch, and F.
823 Weiler, 2020: First validation of Aeolus wind observations by airborne Doppler Wind Lidar
824 measurements. *Atmos. Meas. Tech. Discuss.*, https://doi.org/10.5194/amt-2019-432, in
825 review.

826 **Tables**

827 Table 1: Overview of research campaigns with quantitative comparisons of dropsonde and DWL

828 wind speeds following Witschas et al. (2020).

Campaign	Year	Bias / [m s^{-1}]	Standard deviation/ [m s^{-1}]	Number of observations	Reference
NAWDEX	2016	0.05	1.87	529	
WindVal	2015	-0.03	1.46	938	Reitebuch et al. (2017)
SALTRACE	2013	0.08	0.92	1329	Chouza et al. (2016)
A-TREC	2003	1.2	0.00	740	Weissmann et al. (2005)

829

852   • FIG. 4. Meteosat SEVIRI satellite image at 0830 UTC, 23 Sep 2016 superimposed by

853   flight track of HALO (white) and DLR Falcon (red and orange for the coordinated flight

854   leg between 0800 and 0900 UTC). The satellite image matches with the mid-point in time

855   of the coordinated leg when the aircraft reached the outflow of cyclone Vladiana.

856   • FIG. 5: (a, b) DWL (colored areas), dropsonde (colored observations along arrows) and

857   in situ (colored line contour on top of DWL observations) wind observations and the

858   respective differences to short-range forecast fields of (c) the ECMWF IFS and (d) the

859   Met Office MetUM on 23 Oct 2016. (a) shows observations along the complete flight

860   while (b, c, d) show a subsection indicated by the dark grey box in (a). (b, c, d) are

861   superimposed by potential temperature (black contours) and dynamical tropopause (2

862   PVU, thick black contour) from IFS (b, c) and MetUM (d). Colored dots at the top of

863   each dropsonde agree with dropsonde marks in Fig. 3.

864   • FIG. 6. As in Fig. 5 (b, c, d) but with PV (colored) as represented in the ECMWF IFS (a)

865   and Met Office MetUM (b).

866   • FIG. 7. Observed and modelled wind speeds for dropsonde (lines) and DWL profiles

867   (dots): (a, g) observations, (b, h) IFS, (c, i) differences to IFS, (d, j) observations, (e, k)

868   MetUM and (f, l) differences to MetUM. Distributions with respect to altitude (a-f) and in

869   tropopause relative altitudes (g-l) using the respective dynamical tropopause of IFS (g-i)

870   and MetUM (j-l). Lidar profiles are closest to the dropsondes at the release time and color

871   coding represents color coding as shown in Fig. 3 and 5.

872   • FIG. 8. Magnitude of the vertical shear in vector wind for (a) DWL (colored areas) and

873   dropsonde (colored observation along arrows, see also Figs. 3 and 5), (b) the ECMWF

874   IFS and (c) the Met Office MetUM (subset region is indicated in Fig. 5a) on 23 Oct 2016.

875   Thick black contour marks the dynamical tropopause of the IFS (a, b) and (c) MetUM.

876 • FIG. 9. Distributions of wind speed (a, b) and magnitude of vertical wind shear (c, d) in

877   tropopause-relative coordinates for the subset of the research flight on 23 Sep 2016

878   shown in Fig. 8. Box-whisker plots for distributions of the DWL observations (blue), the

879   IFS (orange) and the MetUM (red). Mean values are shown by the white lines on the box-

880   whiskers and the colored dots. Black diamond markers on the right hand axes indicate

881   statistical significant difference of the medians at the 95% confidence interval using a

882   Wilcoxon Rank-Sum test.

883 • FIG. 10. Histograms of (a, b) DWL wind speed (color shading) and (e, f) DWL wind

884   shear magnitude in 1 km altitude bins relative to the (a, e) IFS and (b, f) MetUM

885   dynamical tropopause. Histograms of differences between analysis/short-term forecasts

886   of ECMWF IFS and DWL and Met Office MetUM and DWL wind speeds (c, d) and

887   wind shear magnitude (g, h). Black (grey) solid line shows median (mean) value of the

888   DWL observations (a,b and e,f) and the differences (c,d and g,h)in each altitude bin.

889   Black (grey) dashed line in a,b and e,f show median (mean) values from the NWP

890   forecast in each altitude bin. Red line indicates the data availability in each altitude bin.

891   Black diamonds markers indicate altitude bins with median differences that are

892   statistically significant using the 95 % confidence intervals calculated from 1000

893   bootstrapping samples.

894

895   •   FIG. 11. Histogram of the differences between modelled and observed wind speeds for

896   (a) IFS and (b) MetUM for all altitude bins (dark grey lines) shown in Fig. 10. The

897   distribution for all observations is shown as blue line and the bin representing the first

898   kilometer above the tropopause by the orange line.

899   •   FIG. 12. Time series of (a) STP wind speeds (in m s^{-1}) at a 6 hourly time resolution

900   measured at South Uist Scotland and (b, c, d) the differences of modelled and observed

901   winds (in m s^{-1}). (b) uses +06 h MetUM forecasts, (c) MetUM operational analyses and

902   (d) IFS operational analyses winds. All panels are superimposed by potential temperature

903   (thin contours) and the dynamical tropopause (2 PVU contour) of ECMWF (a, d) and

904   Met Office (b, c). The dashed line in (a) represents the Met Office dynamical tropopause.

905   •   FIG. A1. (a, b) as in Fig. 10a,c and (c, d) as in Fig. 10e,g but for the WindVAL-I

906   campaign conducted from Iceland in May 2015.

908
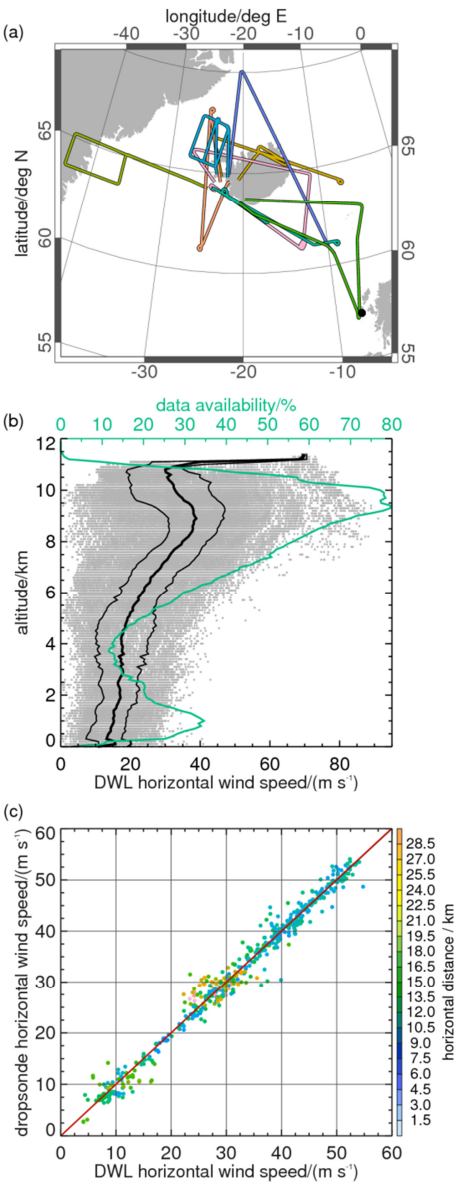
FIG. 1. (a) Location of DWL wind observations during DLR Falcon flights RF02 to RF09. Black

dot marks wind profiler at South Uist, Scotland. (b) Horizontal wind speed vs. altitude for all

DWL observations (grey dots). Average winds (thick black line), 25/75 % percentile (thin black

lines) and data availability (green line) for each 100 m range gate. (c) Comparison of collocated

DWL and dropsonde wind speeds color-coded by horizontal distance between the observations.

Red line shows the linear regression line.

915
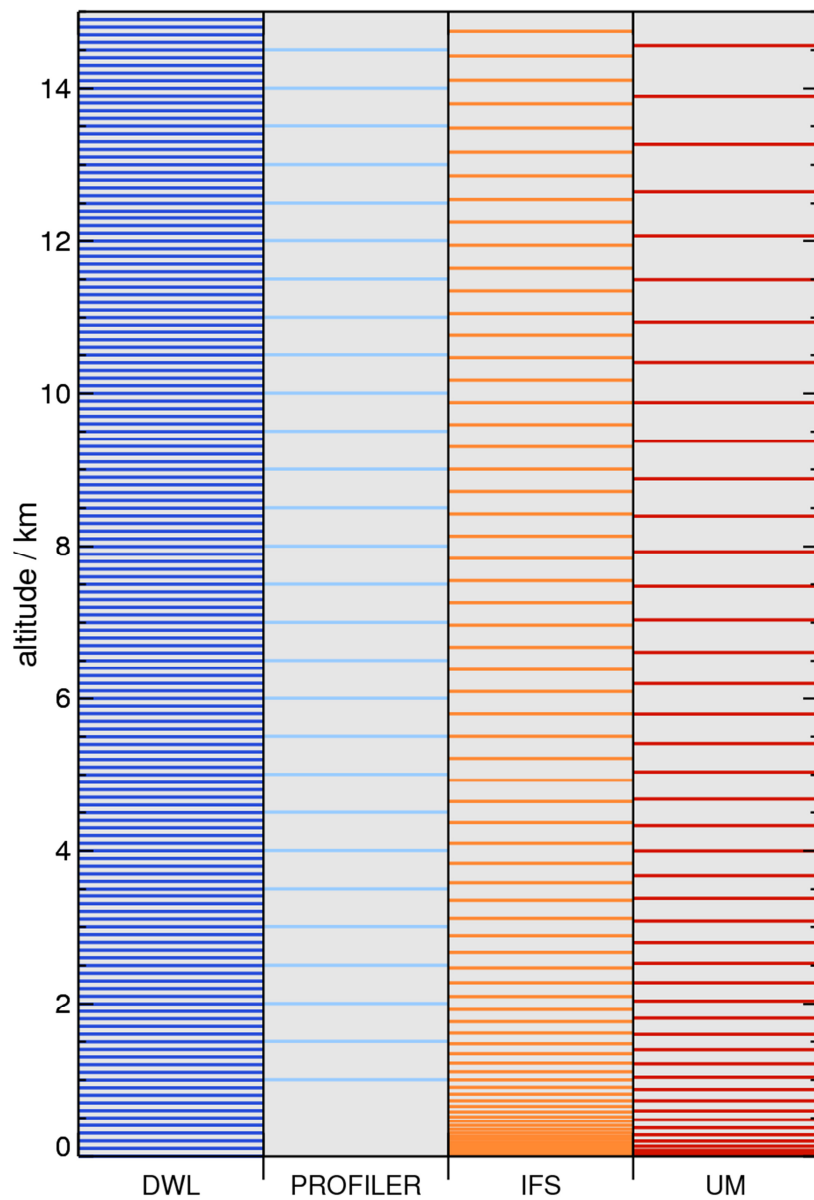
FIG. 2. Vertical distribution of observed and modelled wind data for the DWL (dark blue), the wind profiler at South Uist, Scotland (light blue), the ECMWF IFS (orange) and the Met Office MetUM model (yellow). Please note that IFS model level altitudes vary with surface pressure and temperature profile. The model level distribution is obtained by averaging altitudes for all analysis times (0000, 0600, 1200, 1800 UTC) over South Uist for the period 10 Sep to 19 Oct 2016.

922
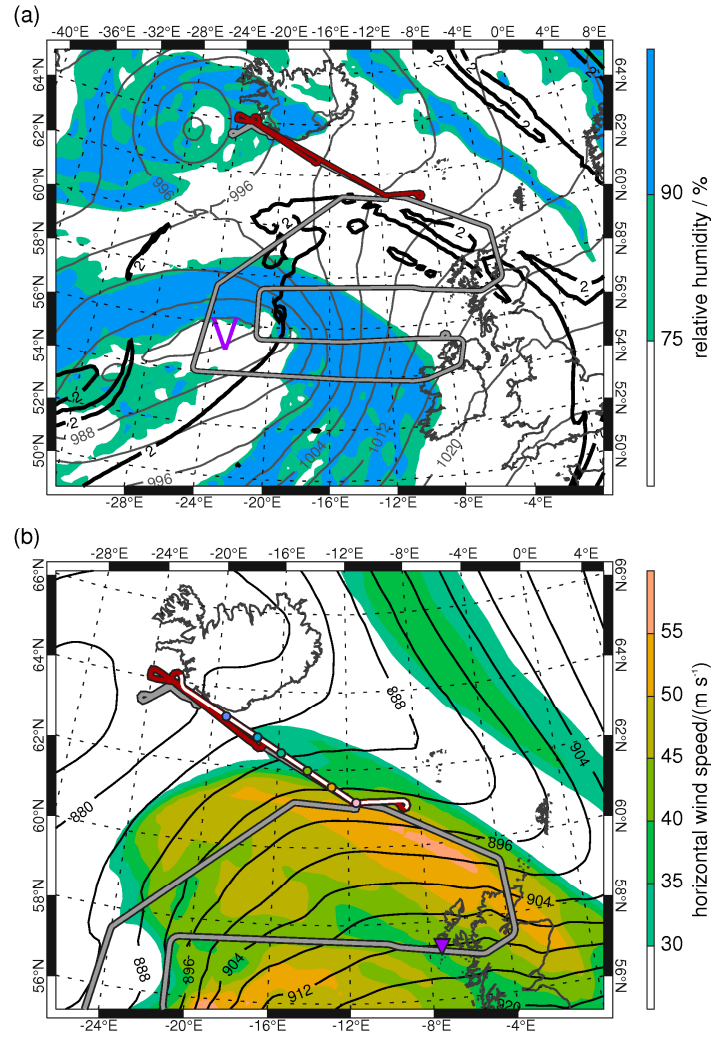
FIG. 3. ECMWF IFS operational forecast for 23 Sep 2016, 0900 UTC (+09 h): (a) Relative humidity at 700 hPa (color shading), 2 PVU at 320 K (thick black contour) and mean sea level pressure (thin grey contours, in hPa). Purple V indicates the position of cyclone Vladiana. (b) Horizontal wind speed (color shading) and geopotential height (black contours, in dm) at 300 hPa. (a) and (b) are superimposed by flight tracks of the DLR Falcon (0710–1020 UTC, red line) and HALO (0736–1636 UTC, grey line) and (b) shows the coordinated leg between 0800 and 0900 UTC (white line). Colored dots mark the position of six dropsondes released from HALO. Purple triangle shows location of South Uist wind profiler.

931
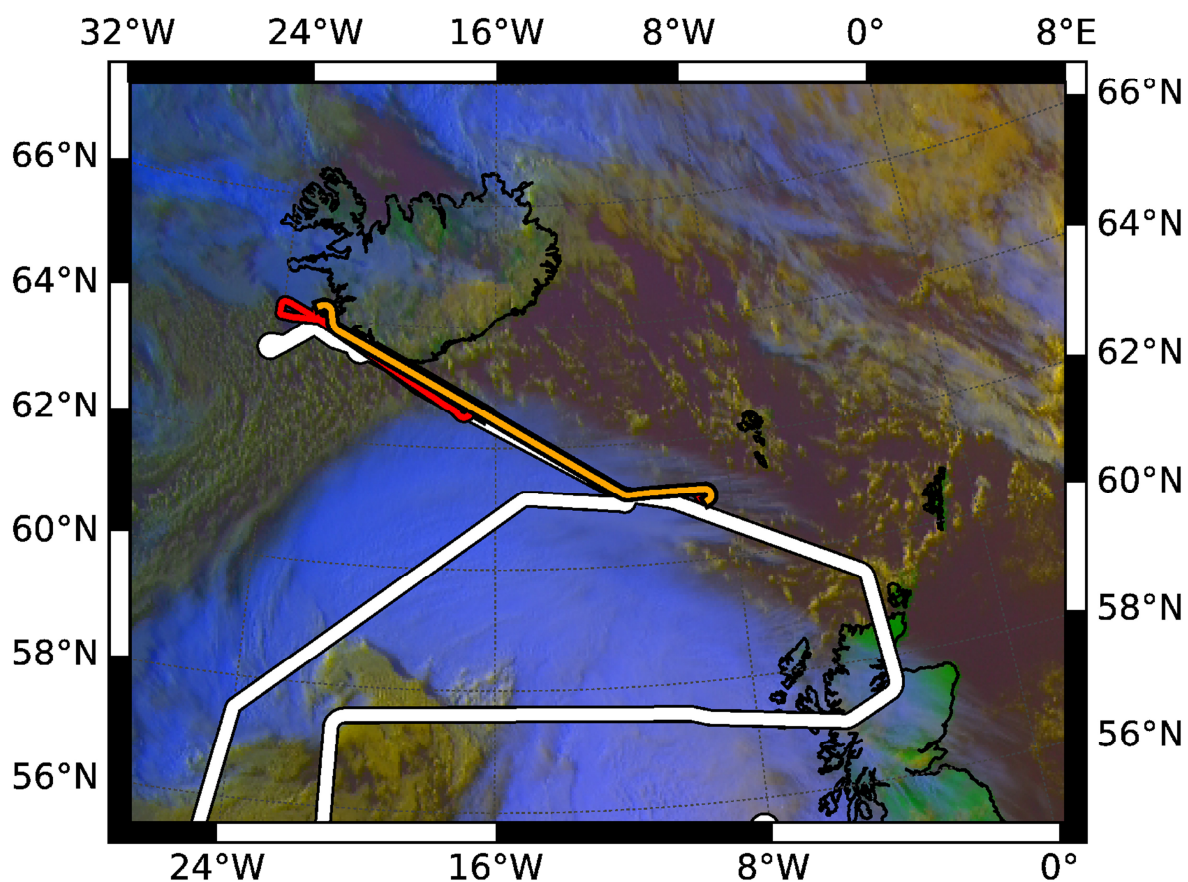
FIG. 4. Meteosat SEVIRI satellite image at 0830 UTC, 23 Sep 2016 superimposed by flight track

of HALO (white) and DLR Falcon (red and orange for the coordinated flight leg between 0800

and 0900 UTC). The satellite image matches with the mid-point in time of the coordinated leg
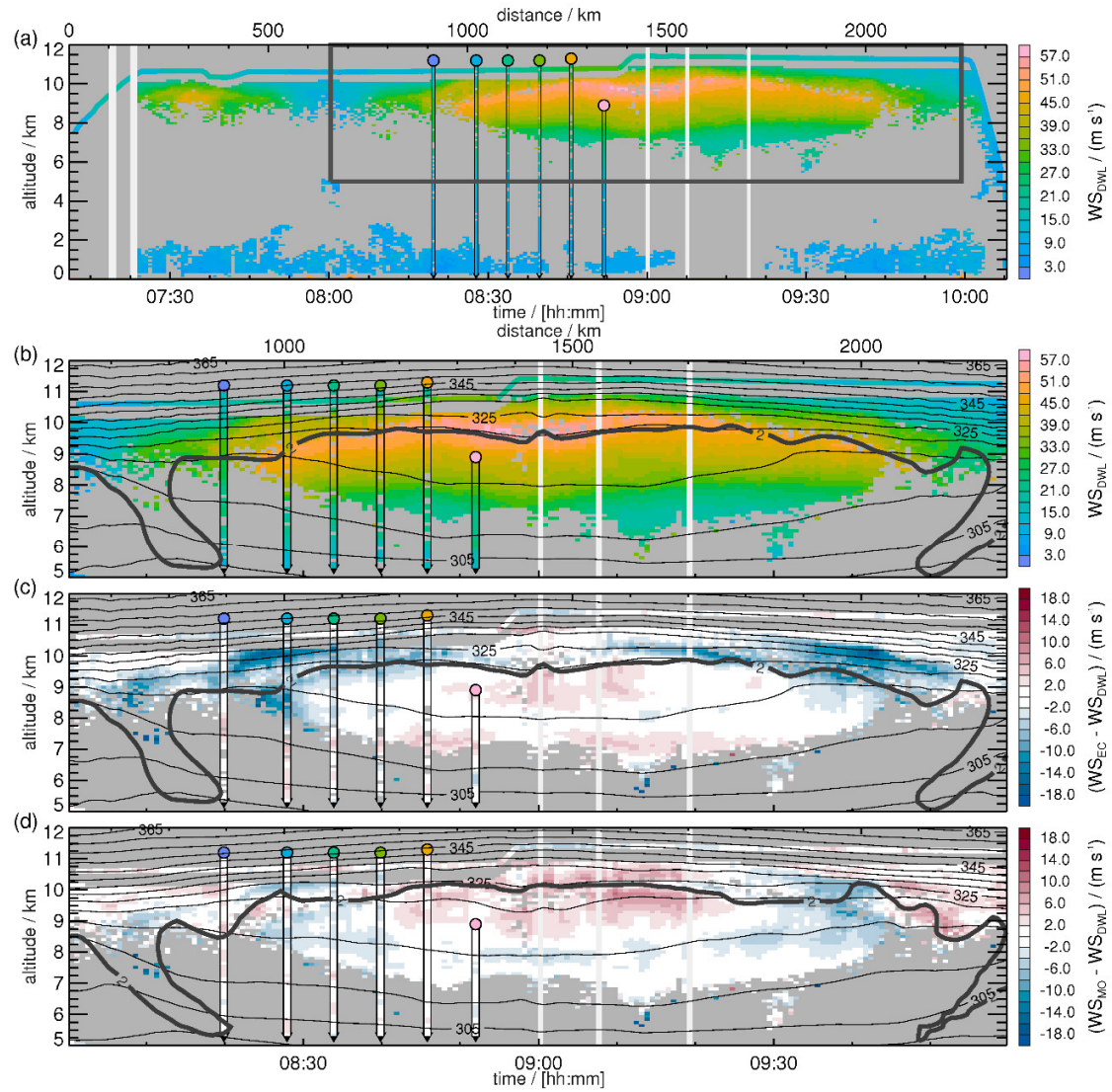
when the aircraft reached the outflow of cyclone Vladiana.

936

FIG. 5. (a, b) DWL (colored areas), dropsonde (colored observations along arrows) and in situ (colored line contour on top of DWL observations) wind observations and the respective differences to short-range forecast fields of (c) the ECMWF IFS and (d) the Met Office MetUM on 23 Oct 2016. (a) shows observations along the complete flight while (b, c, d) show a subsection indicated by the dark grey box in (a). (b, c, d) are superimposed by potential temperature (black contours) and dynamical tropopause (2 PVU, thick black contour) from IFS (b, c) and MetUM (d). Colored dots at the top of each dropsonde agree with dropsonde marks in Fig. 3.

945
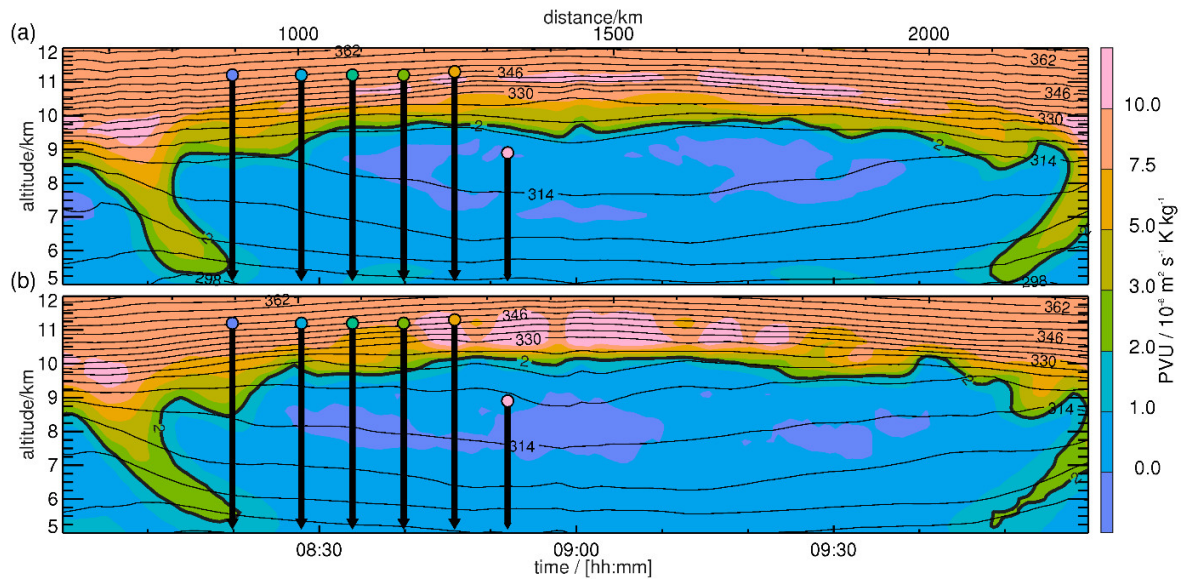
FIG. 6. As in Fig. 5 (b, c, d) but with PV (colored) as represented in the ECMWF IFS (a) and
Met Office MetUM (b).
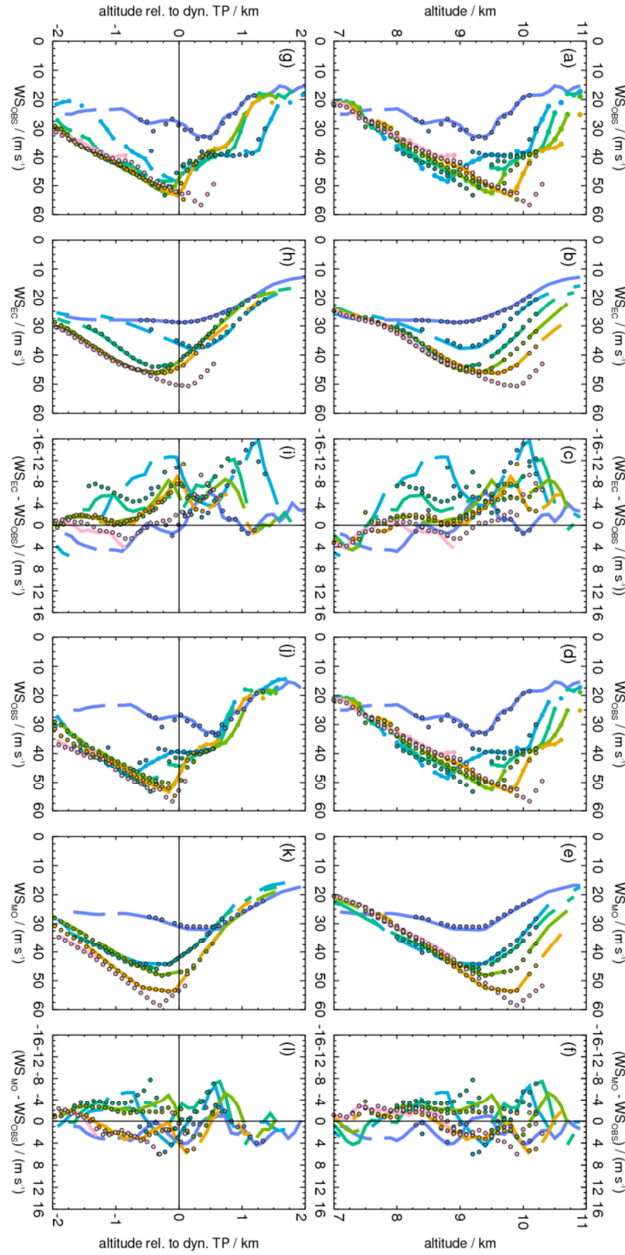
FIG. 7. Observed and modelled wind speeds for dropsonde (lines) and DWL profiles (dots): (a, g) observations, (b, h) IFS, (c, i) differences to IFS, (d, j) observations, (e, k) MetUM and (f, l) differences to MetUM. Distributions with respect to altitude (a-f) and in tropopause relative altitudes (g-l) using the respective dynamical tropopause of IFS (g-i) and MetUM (j-l). Lidar profiles are closest to the dropsondes at the release time and color coding represents color coding as shown in Fig. 3 and 5.
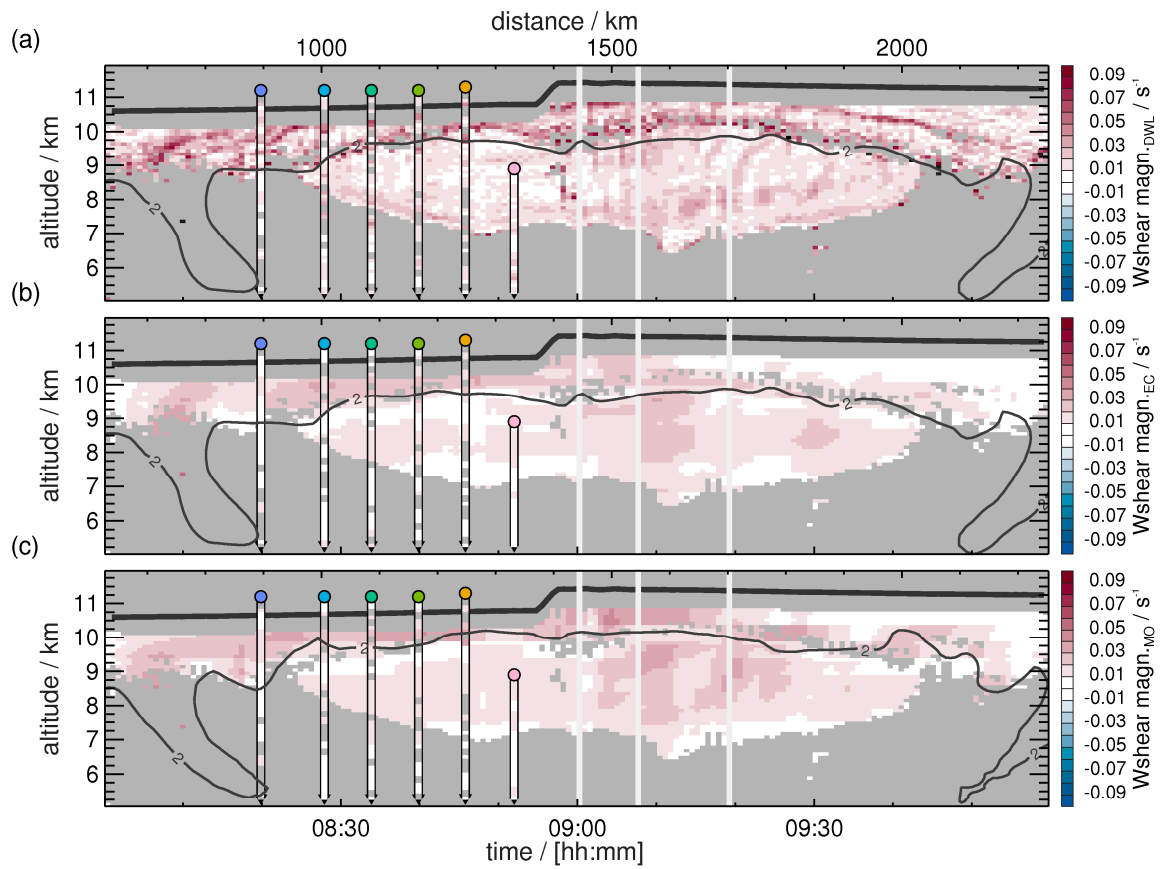
FIG. 8. Magnitude of the vertical shear in vector wind for (a) DWL (colored areas) and dropsonde (colored observation along arrows, see also Figs. 3 and 5), (b) the ECMWF IFS and (c) the Met Office MetUM (subset region is indicated in Fig. 5a) on 23 Oct 2016. Thick black contour marks the dynamical tropopause of the IFS (a, b) and (c) MetUM.
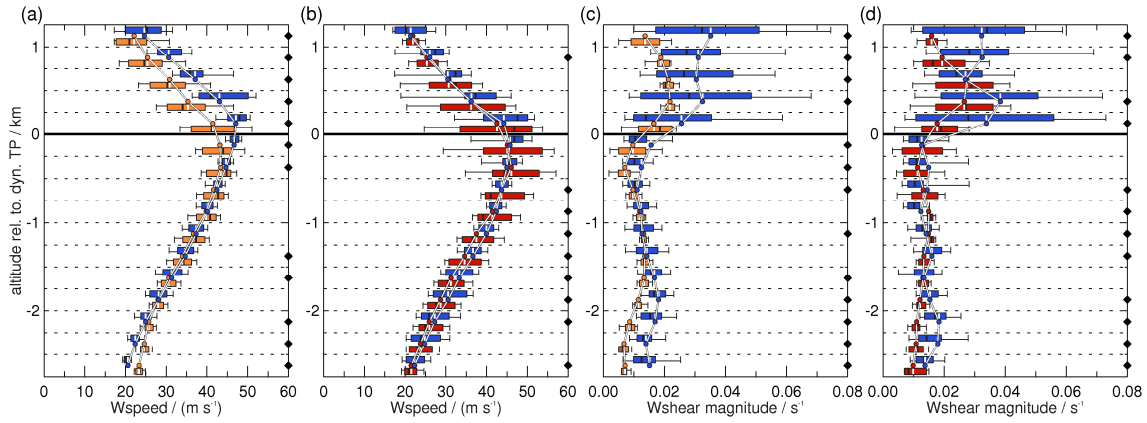
FIG. 9. Distributions of wind speed (a, b) and magnitude of vertical wind shear (c, d) in tropopause-relative coordinates for the subset of the research flight on 23 Sep 2016 shown in Fig. 8. Box-whisker plots for distributions of the DWL observations (blue), the IFS (orange) and the MetUM (red). Mean values are shown by the white lines on the box-whiskers and the colored dots. Black diamond markers on the right hand axes indicate statistical significant difference of the medians at the 95% confidence interval using a Wilcoxon Rank-Sum test.
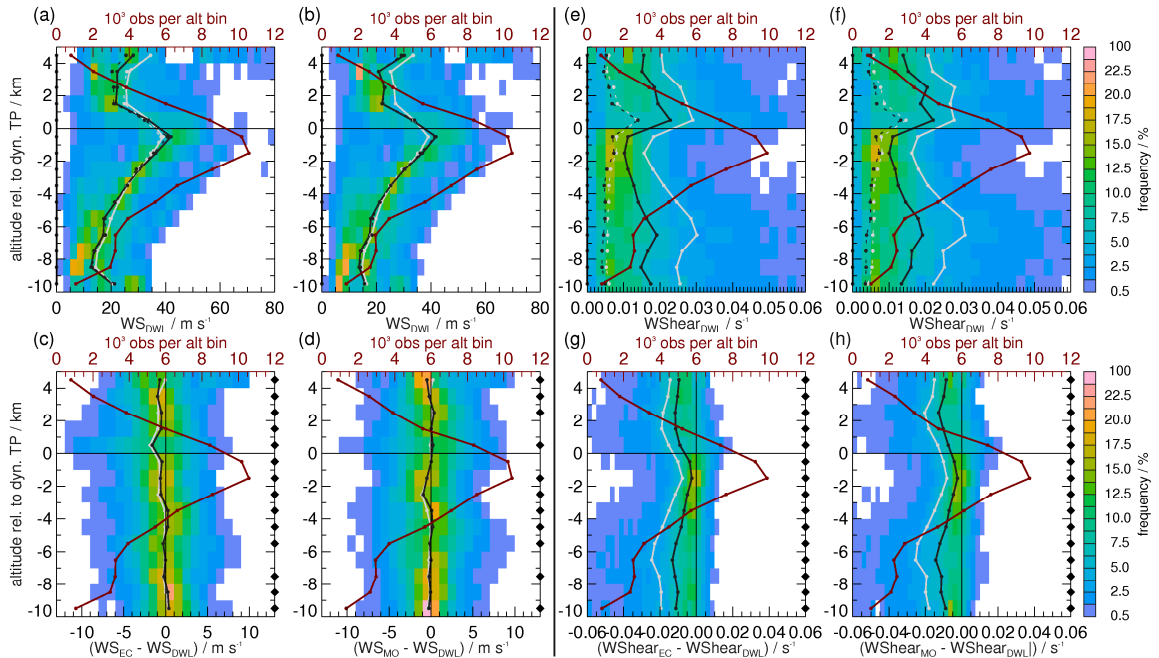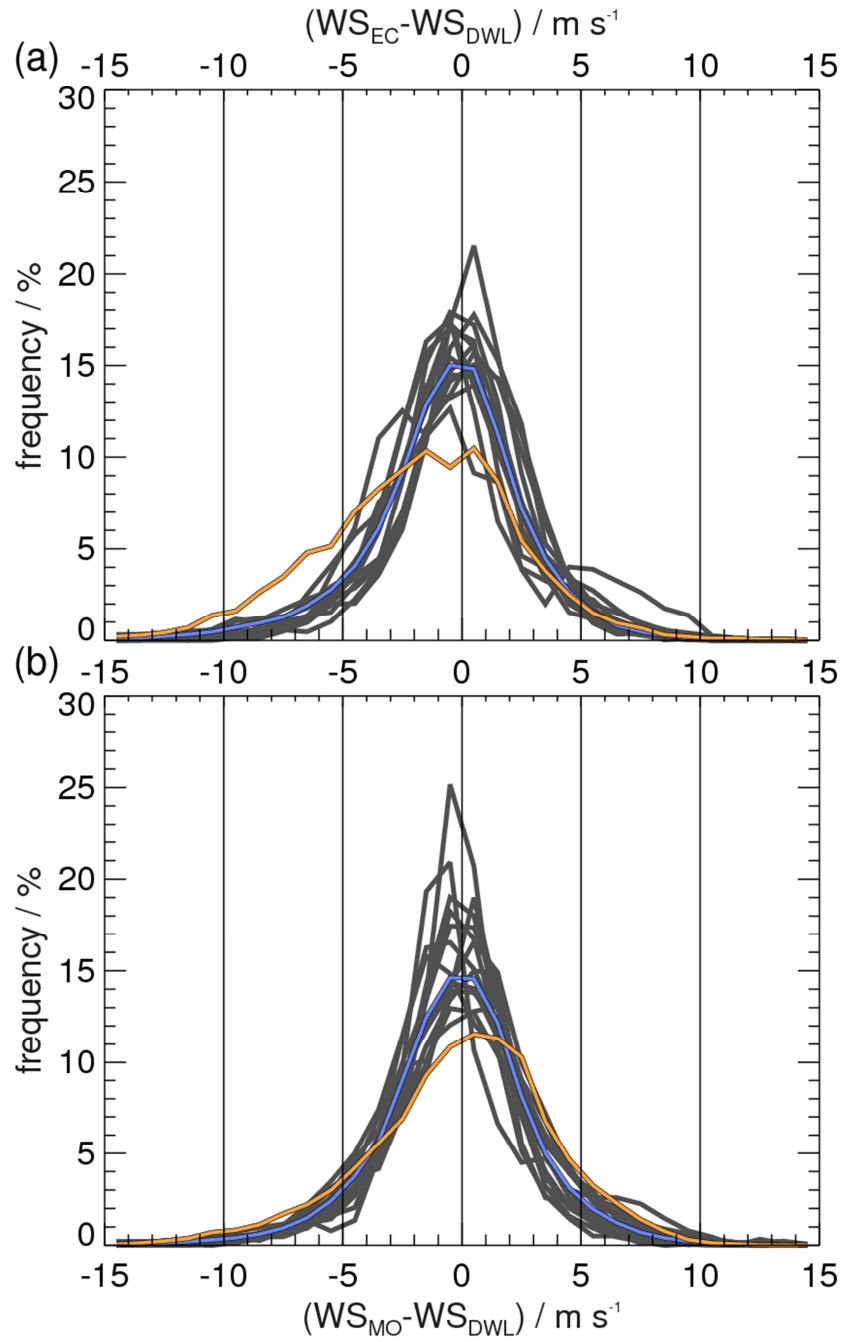
969 FIG. 10. Histograms of (a, b) DWL wind speed (color shading) and (e, f) DWL vertical wind

970 shear magnitude in 1 km altitude bins relative to the (a, e) IFS and (b, f) MetUM dynamical

971 tropopause. Histograms of differences between analysis/short-term forecasts of ECMWF IFS and

972 DWL and Met Office MetUM and DWL wind speeds (c, d) and vertical wind shear magnitude

973 (g, h). Black (grey) solid line shows median (mean) value of the DWL observations (a,b and e,f)

974 and the differences (c,d and g,h)in each altitude bin. Black (grey) dashed line in a,b and e,f show

975 median (mean) values from the NWP forecast in each altitude bin. Red line indicates the data

976 availability in each altitude bin. Black diamonds markers indicate altitude bins with median

977 differences that are statistically significant using the 95 % confidence intervals calculated from

978 1000 bootstrapping samples.

FIG. 11. Histogram of the differences between modelled and observed wind speeds for (a) IFS and (b) MetUM for all altitude bins (dark grey lines) shown in Fig. 10. The distribution for all observations is shown as blue line and the bin representing the first kilometer above the tropopause by the orange line.

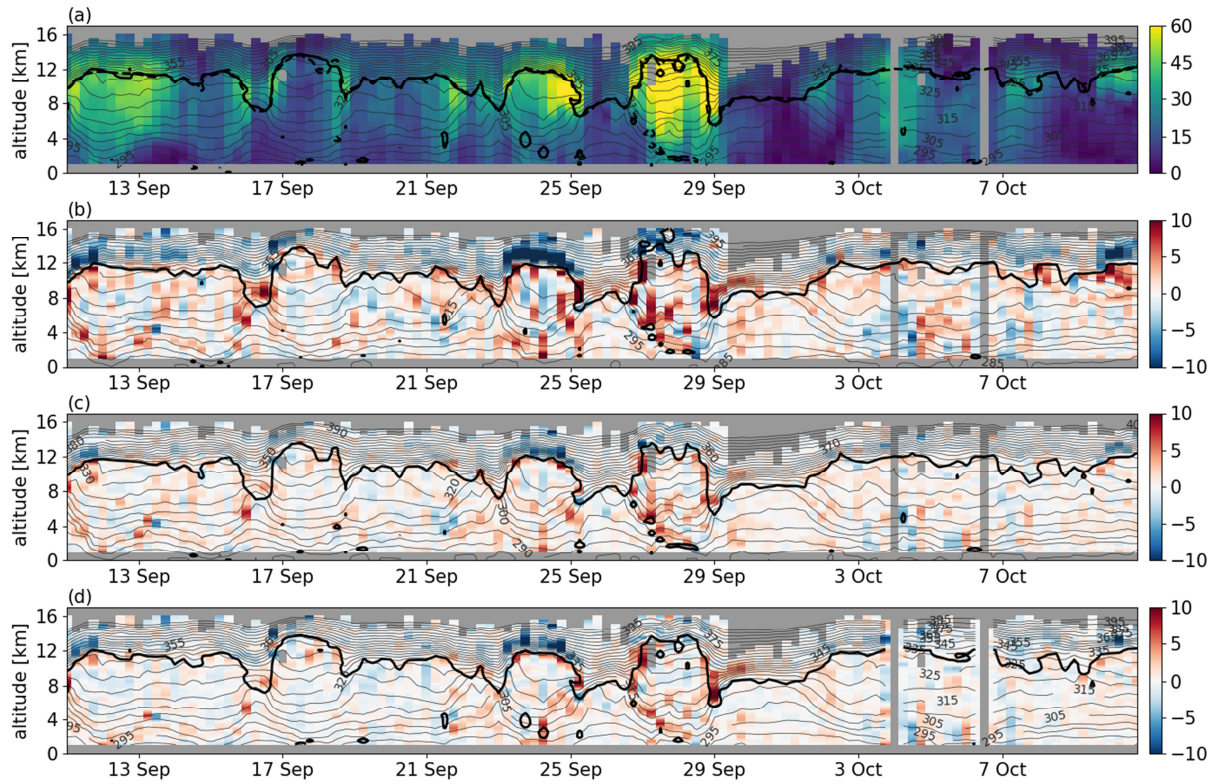FIG. 12. Time series of (a) STP wind speeds (in m s^{-1}) at a 6 hourly time resolution measured at South Uist Scotland and (b, c, d) the differences of modelled and observed winds (in m s^{-1}). (b) uses +06 h MetUM forecasts, (c) MetUM operational analyses and (d) IFS operational analyses winds. All panels are superimposed by potential temperature (thin contours) and the dynamical tropopause (2 PVU contour) of ECMWF (a, d) and Met Office (b, c). The dashed line in (a) represents the Met Office dynamical tropopause.
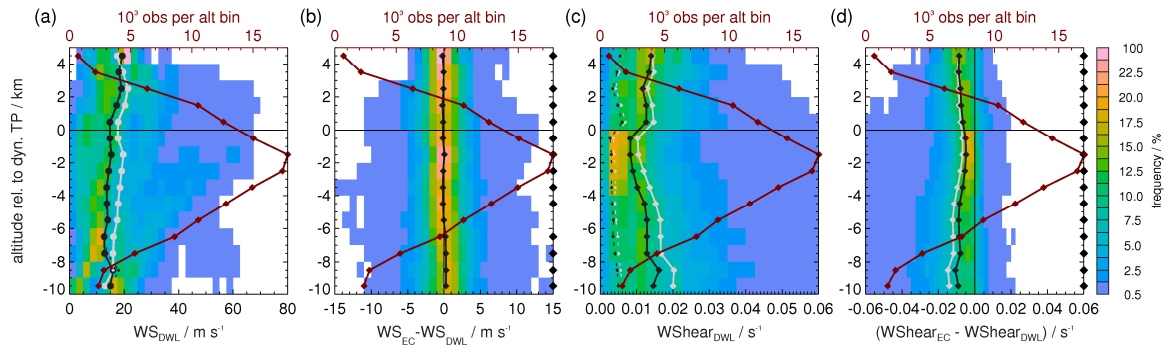
992

993 FIG. A1. (a, b) as in Fig. 10a,c and (c, d) as in Fig. 10e,g but for the WindVAL-I campaign

994 conducted from Iceland in May 2015.